Chapter IV

Ni/Co stacked MOFs as a nano-electronic transducer integrated with smartphone for nitrite sensing in environmental water samples

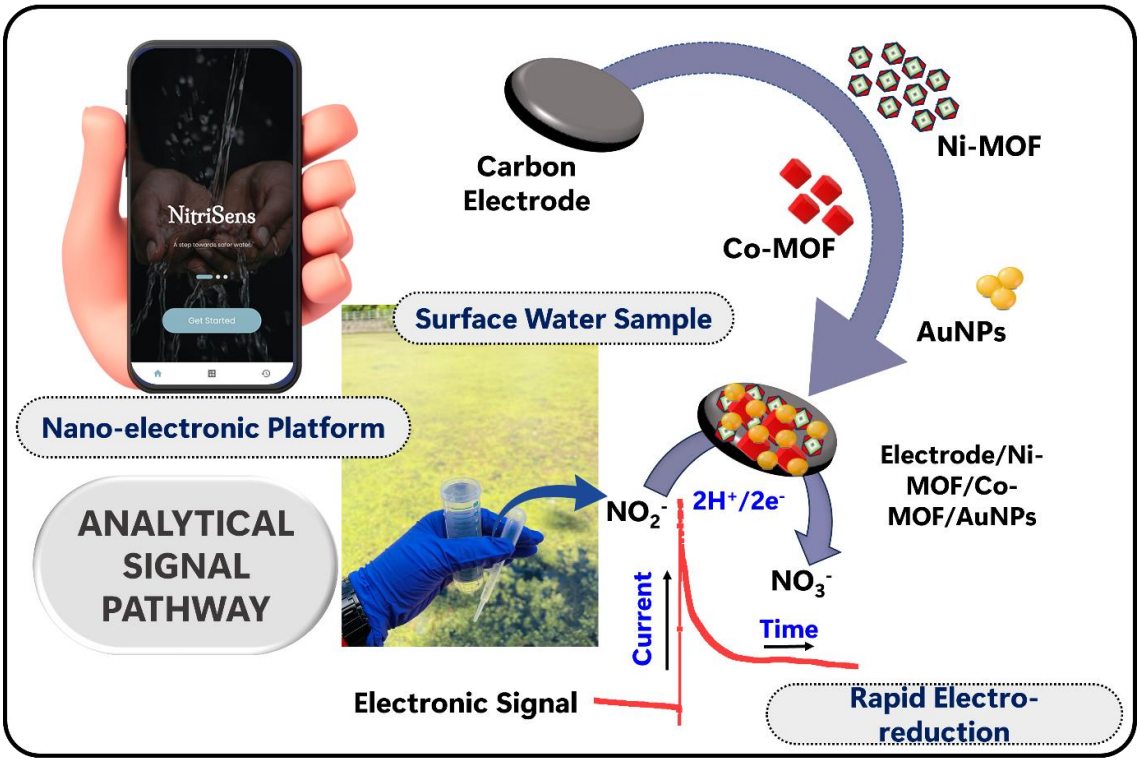

Shubhangi et al., ACS Applied Electronic Materials, 2025 (Revision Submitted)

1. Introduction

Sensitive detection of nitrite (NO_2^-), a heavily talked about environmental menace, is important due to its detrimental effects on humans and other living beings[1]. Anthropogenic activities (use of nitrogenous pesticides) and discharge of industrial effluents in water bodies has resulted in the surge of its concentration in ground water too[2]. It also finds its widespread usage in food preservation industries where its prevents food spoilage by species such as *Clostridium botulinum*[3]. Nevertheless, its highest exposure to humans remains through ingesting its high dosage through the medium of food and water. Some of the untreated foods such as beets, potatoes and tomatoes inherently contain low concentrations of NO_2^- [3]. When at high concentrations, it combines with haemoglobin in blood restricting oxygen supply to cells, a phenomenon called as the 'blue baby syndrome' in newborns[4], making drinking water nitrite concentration an important concern in infants. Its known conversion from nitrite to nitrosamines, a known carcinogen, necessitates its sensitive detection in water and food in current world. Lethal concentrations of NO_2^- in drinking water as per WHO guidelines falls above 65µM, forcing industry to adapt newer methods to estimate nitrite in water bodies since a longtime[5]. There have been different methods reported for NO_2^- detection such as capillary electrophoresis[6], spectrophotometry[7], chromatography[8], chemiluminescence[9] and sequential injection[10]. It is also important to understand that most of the listed methods however are expensive, require hefty machinery, derivatization, large solution processing time and profound expertise, limiting their deployment for on-site detection. An easier, faster and cheaper approach is the electrochemical estimation which is now being explored for its sensitive sensing in wide matrices[11,12]. Unmodified electrodes can detect NO_2^- but suffer from large overpotential, demanding suitable electrode modifications for their commercial sensing utility[13].

Metal organic frameworks (MOFs) are evolving 2D and 3D microporous materials which have recently found their utility in several applications including the trending roles in electrochemical sensing matrices[14]. They find their purpose as surface area enhancing moieties enabling functionalization along with the catalytic roles often played by their metal centers[14]. Their roles advance with integration of metal nanoparticles (NPs) by facilitating reduction in their agglomeration and increment in NP stability[15]. However, the current challenges for MOFs still resides in their poor stability within a range of solvent and media systems, complex synthesis routes involving high temperature and compromised charge transfer characteristics[15]. Again, as sensor matrix component, MOFs often lead to compromised conductivity, poor limit of detection (LOD), limited linear dynamic range (LDR) and low sensitivity. To address these problems, they are often adorned with quantum dots or NPs to elevate sensor performance and sensitivity towards the target analyte[16,17]. Specifically in case of our analyte of interest, the usage of AuNP was imperative with the fact that Au binds with nitrite, thereby oxidizing and sensing it at lower potential values, as suggested by numerous reports[18,19].

The current work attempts at exploiting the porous architecture of MOFs with catalytic metal centers (Ni-MOF stacked upon Co-MOF) to accommodate and adhere AuNP, yielding synergistic outcomes for effective NO_2^- oxidative sensing. The work focusses on the fabrication of the above versatile system over the surface of a glassy carbon electrode (GCE) followed by its extensive physical and electrochemical characterization and thereafter utility as a sensing matrix against NO_2^- in real water samples collected from pond and local community supply. The sensor has been further integrated with a smart-phone platform providing an on-site NO_2^- estimation tool giving its concentration in nM in no time. This is the first report on stacking two highly catalytic metal-centered MOFs

and integration of smart-phone interface for automated and user-friendly sensing of NO_2^- **(Figure 4.1).**

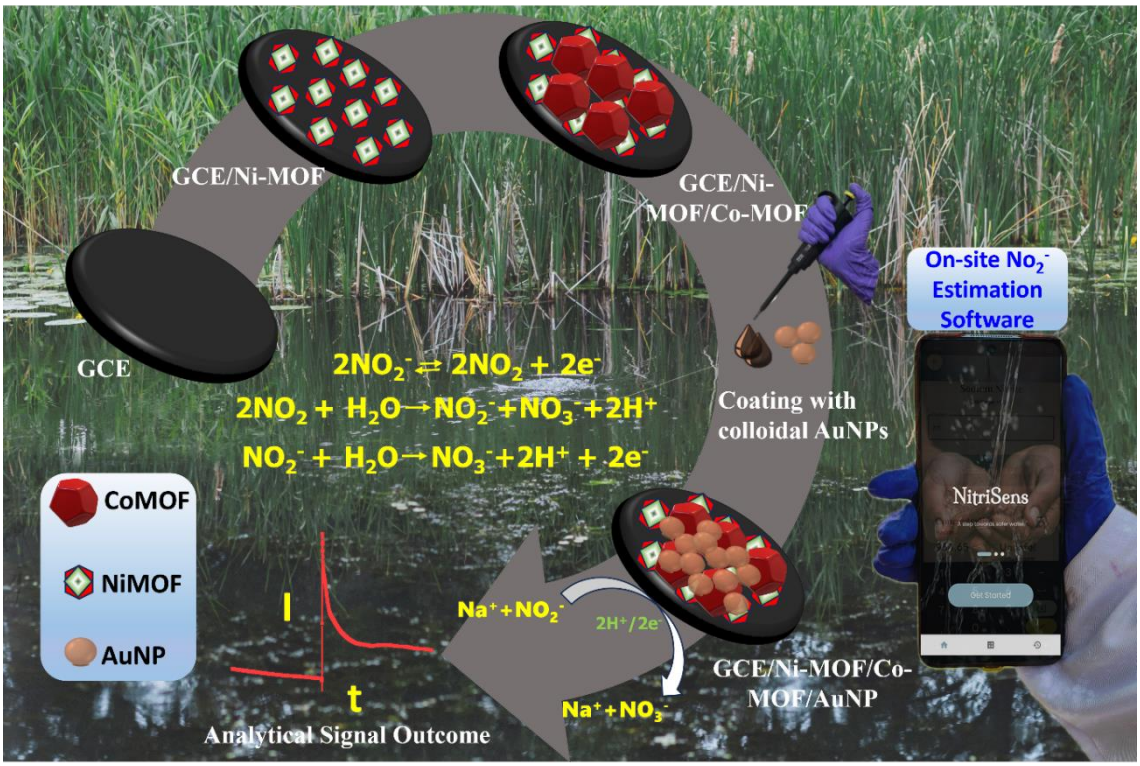

Figure 4.1. *A schematic representation of the fabrication strategy adopted to develop the nitrite sensing and thereby its estimation module involving a smartphone-integration.*

2. Materials and Methods

2.1. Chemicals and Instruments

All chemicals and reagents used in the study are of the analytical grade, in their purest form. ZoBell's electrolytic solution (ZS) ($K_3[Fe(CN)_6]/K_4[Fe(CN)_6]$), 5mM; pH-7 was prepared using Potassium hexacyanoferrate (III) ($K_3Fe(CN)_6$) and potassium hexacyanoferrate (II) ($K_4Fe(CN)_6$) were purchased from Himedia Pvt. Ltd., India. $NaNO_2$ was obtained from Sisco Research Pvt. Ltd. (SRL), India. All standard solutions, like phosphate buffer saline (PBS) and ZS were prepared in-house using double-distilled water which was obtained from a Milli-Q water purifier (water resistance 18.2 MΩ). PBS was prepared using sodium monophosphate (NaH_2PO_4), sodium bisphosphate (Na_2HPO_4), and sodium chloride (NaCl), bought from SRL, India. The MOF precursor

solutions were prepared using the nickel nitrate hexahydrate ($Ni(NO_3)_2.6H_2O$), cobalt nitrate hexahydrate ($Co(NO_3)_2.6H_2O$), and 2 methyl-imidazole(Me-Im) in dimethyl formamide (DMF), all procured from SRL, India. AuNP preparation involved usage of chloroauric acid ($HAuCl_4$) and trisodium citrate which were purchased from SRL, India. Tap water was obtained from the local water supply pipeline available to nearby household and pond water samples were obtained from local pond present within premises of Indian Institute of Technology (BHU).

All physical characterization tools were availed at the Central Instrument Facility Centre (CIFC), IIT (BHU). HR-SEM results were obtained using the Nova Nano SEM 450 by FEI, EDS by EDAX Inc., and the EVO - Scanning Electron Microscope MA15 / 18, CARL ZEISS Microscopy Ltd. and the XPS using the K-Alpha, by Thermo-Fisher Scientific. For all the electrochemical measurements, an electrochemical workstation (Palm Sens 4.0, Houten, Netherlands) was deployed. It comprised of a three-electrode system with Ag/AgCl as the reference, Pt wire as the counter and GCE as the working electrode in the current set of experiments.

2.2. Fabrication of the GCE/NiMOF/CoMOF/AuNP sensing platform

The GCE was initially pre-treated as per the standard protocol to remove all impurities[20]. Then, it was dipped into the standard Ni-MOF precursor solution comprising of 50 mM $Ni(NO_3)_2.6H_2O$ and 75 mM of 2-MeIm dissolved and stirred in 10 ml DMF solvent system. The deposition of the Ni-MOF was done using chronoamperometry (CA) at a deposition potential of -1.4 V vs. Ag/AgCl for a duration of 400 seconds, using optimized CA parameters. Then, the obtained probe was rinsed and dried for few minutes to further coat it with the next layer of the Co-MOF. The Co-MOF precursor solution was prepared likewise as the former MOF by dissolving 50 mM $Co(NO_3)_2.6H_2O$ and 75 mM of 2-MeIm in 10 ml DMF and stirring at room temperature for 5 minutes. After preparing the

precursor solutions, the modified GCE/Ni-MOF electrode was dipped into this solution and electrodeposited at an optimized potential of -1.4 V vs. Ag/AgCl to obtain the Co-MOF over it. It is important to understand that optimization of the deposition time is also an important aspect to obtain the Co-MOF with the desired charge transfer characteristics and morphology, which has been discussed in detail in the upcoming section.

On further rinsing of the GCE/Ni-MOF/Co-MOF with distilled water post deposition, the final layer of the probe, i.e. colloidal AuNP prepared through the standard citrate method[21], was coated onto the sensor surface. 4 µl of the synthesized colloidal AuNP were coated onto the GCE/Ni-MOF/Co-MOF surface and allowed to dry at room temperature for 15 minutes. Then, upon drying, the final surface was mildly rinsed with distilled water to obtain the desired sensing surface. The electrode was stored in desiccator till further usage. The confirmation of the metal centers in the stacked MOFs and the gold in the AuNP layer was first concluded through the EDX analysis, mapping, and XPS results. Further, the confirmation of metallic presence in the sensor matrix was validated through electrochemical estimation in respective electrolytic solutions. Thereafter, individual layers of the final sensing surface have also been fabricated and evaluated in order to determine the effectiveness of each surface.

2.3. Electrochemical Evaluation of the GCE/NiMOF/CoMOF/AuNP sensing platform

The electrochemical characterization of the final sensing matrix was done by dipping the electrodes in ZS solution, undergoing analysis through various electrochemical measurements such as cyclic voltammetry (CV) and electrochemical impedance spectroscopy (EIS). The measurement parameters have been mentioned appropriately at places of relevant discussions. The results of EIS were acquired at an open-circuit potential with a frequency between 10 to 104 Hz. The LSV and chronoamperometric

signals were recorded between a potential range of +0.4 V to +1.2 V vs. Ag/AgCl and +0.95 V vs. Ag/AgCl, respectively to procure the outcomes for the control studies and the standard calibration plots.

3. Results and Discussion

3.1. The deposition of the stacked MOF over the electrode surface, followed by AuNP functionalization

One of the most promising methods for fabricating MOF is electrodeposition, and in this method, optimizing voltage and deposition time is crucial[22]. At first, the potential and deposition time optimization for the electrodeposited MOFs is a crucial aspect to start the discussion with. The deposition of the Ni-MOF was done referring our previous work with minor changes like alterations in deposition parameters[22]. The deposition time optimization was done varying it between 20-400 seconds, as shown in **Figure 4.2A**. It is interesting to note that the charge transfer characteristics of the layer rises at 150 seconds but drops back a little and finally rises again at 400 seconds **(Figure 4.2B)**. We checked the formed nanostructures for their catalytic potential, however, the most conductive nanostructures formed at 150 seconds were not able to catalyse our target nitrite anions. Therefore, we moved further and found that the ones formed at 400 seconds were the most catalytic species facilitating maximal nitrite conversion and its thereby, detection. Hence, we chose 400 seconds as the optimum time point for Ni-MOF synthesis for catalytic nitrite sensing matrix fabrication.

This was followed by a controlled deposition of the Co-MOF detailed in the current study which is one of its kind. For utilizing the developed electrodeposited MOF for purpose of sensor probe conductivity enhancement and thereby, electro-oxidation of the target analyte, it is important to understand the parameters to obtain maximum conductance of

the deposited layer. The time duration for deposition of Co-MOF was varied from 100 seconds to 1500 seconds **(Figure 4.2C)**. It was interesting to note that with an increase in the electrodeposition time from 100 to 600 seconds, there was a gradual rise in the conductivity of the modified probe however, it became almost constant after 600 seconds till 1500 seconds, as shown in **Figure 4.2D**. Therefore, the deposition time of 600 seconds was chosen as the optimum time to obtain the most conductive form of Co-MOF. There have been previous reports on the electro-deposition of Co-MOF (ZIF-67), through various routes with higher deposition potentials and long deposition times **(Table 4.1)**. It is important to note that this study reports the improved process of Co-MOF electrodeposition in terms of lower potential and shorter deposition time with its strikingly enhanced conductivity posing its utility in molecular sensing applications. It was further investigated that the nanostructures formed at 600 seconds were catalytically potent against our target species. Furthermore, stacking both metallic MOFs on top of one another improved the composites' catalytic properties and overall sensing attributes, as discussed in succeeding sections. Integration with AuNP on the system was done by first synthesising the AuNP through the standard citrate method followed by its coating onto the stacked MOF surface[21]. In brief, 100 ml of 1 mM $HAuCl_4$ was brought to boil and stirred for 30 minutes until 5 ml of 78 mM of trisodium citrate solution was added to it and stirred for another 15 minutes to obtain the wine-red coloured colloidal NP solution. To validate the formation of all the desired surface components and the synchronous activity of the Ni-MOF/Co-MOF/AuNP probe, it was meticulously characterized through a range of physical and electrochemical characterizations tools.

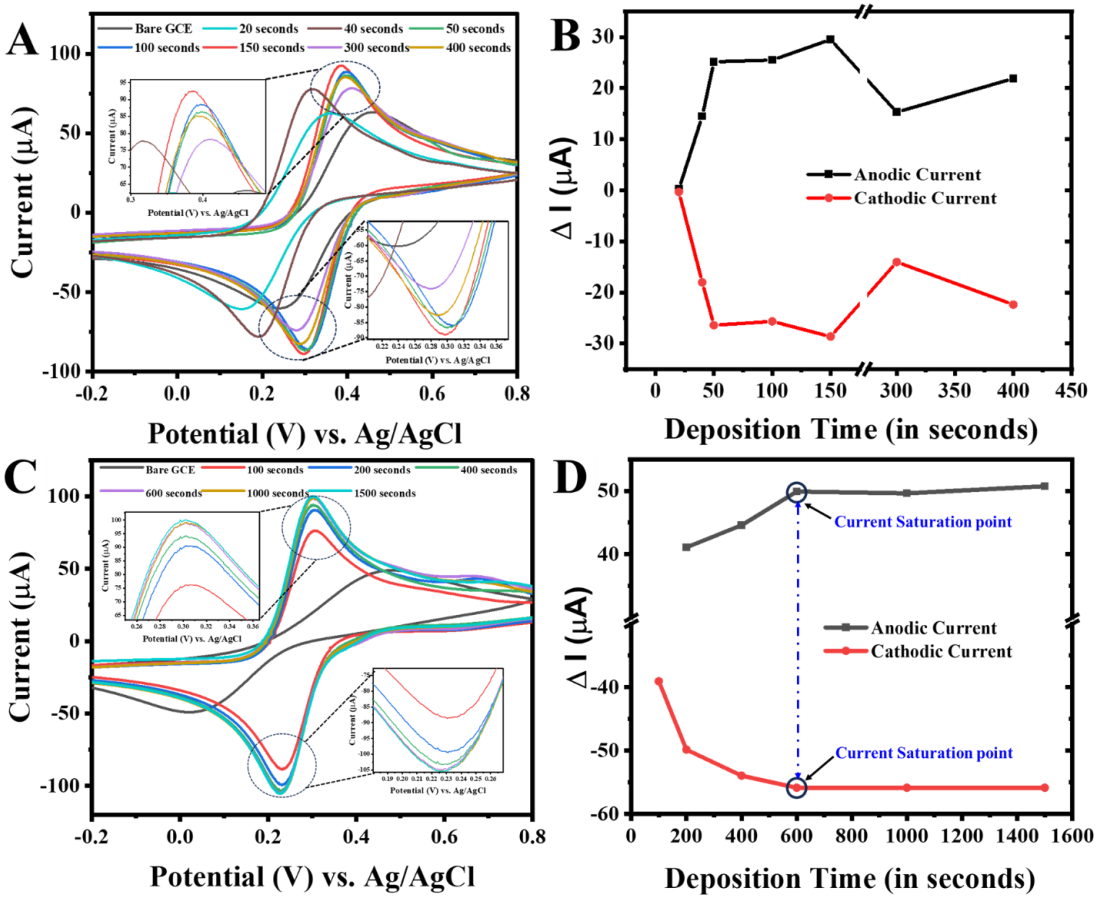

Figure 4.2. *CV curves for optimization of time-dependent deposition of (A) Ni-MOF (B) optimization plot for anodic and cathodic currents obtained at various time points (20-400 seconds) in case of Ni-MOF; (C) Time-dependent deposition of Co-MOF (D) optimization plot for anodic and cathodic currents obtained at various time points in case of Co-MOF (100-1500 seconds).*

Table 4.1. *Co-MOF deposition parameters comparison with previous reports.*

S.No.	MOF composite	Method of fabrication	Precursor salt and its concentration	Precursor linker and its concentration	Solvent system	Reaction conditions	Total time	Reference
1.	ZIF-67	Electrochemical	$Co(NO_3)_2 \cdot 6H_2O$ (0.1 mol/L)	2-MeIm (0.8 mol/L)	Methanol/water (95:5)	Two electrode system WE: Cu mesh CE: Graphite plate V= 5.0 V	200 seconds	[23]
2.	GO-ZIF67	Hybrid	$Co(NO_3)_2$ (0.05 M)	2-methyl imidazole (5.5 g/20 mL H2O)	water	Hybrid method where $Co(OH)_2$ was electrodeposited at -1.0 V (vs. SCE) followed by reaction in at RT, 6 hours	6 hour 30 minutes	[24]
3.	ZIF-67	Electrochemical	Co foil	2-methyl imidazole (0.12–0.24 mol per dm^{-3}) Mediator:MTBAMS: (0.06–0.12 mol per dm^{-3})	DMF/H2O (3:4)	Two metal foil electrodes (Co), V=2.5V	60–300 minutes	[25]
4.	ZIF-67	Solvothermal method at RT	$Co(NO_3)_2 \cdot 6H_2O$ (2.9 g)	2-methylimidazole (6.5 g)	Methanol	RT synthesis followed by separate electrophoretic deposition on FTO coated glass substrate in electric fields ranging from 20 to 60 $V \cdot cm^{-1}$	Not specified	[26]
5.	ZIF-67	Hybrid method	$Co(NO_3)_2 \cdot 6\ H_2O$ (0.5M)	2-Methylimidazole (5 g) was dissolved in deionized water (20 mL)	Water	Electrodeposition of $Co(OH)_2$ nanosheets at −1 V (vs. SCE) for 10 min at (25±1) °C, dried then dipped in 2-MeiM solution for 15 minutes.	10 minutes+12 hours+15 minutes	[27]
6.	ZIF-67	Solvothermal at RT	(Co(NO3)2•6H2O, 3.492g)	2-methylimidazole (3.94 g) was added to the 60 ml mixed solution	ethanol and methanol (V:V =1:1)	Stirring for 20 hours at RT, washing and drying	20 hours	[28]
7.	ZIF-67	Electrodeposition (2 step)	$Co(CH_3COO)_2$ (20 mM)	2-methylimidazole (1M)	.1 M Na_2SO_4	cobalt-modified FTO electrode was prepared on Au electrode at −1.0 V, followed by deposition of ZIF-67 at 0.5 V in the electrolytic solution.	30 minutes	[29]
8.	ZIF-67	Hybrid	0.1 M $Co(NO_3)_2$	2-MeIM (0.5, 1.0, or 2.0 M) was prepared in a mixed solvent of 5 mL H_2O and 5 mL EtOH	Ethanol and water (V:V=1:1)	Cobalt hydroxide ($Co(OH)_2$) was directly deposited on CP at -0.95 V vs. Ag/AgCl, followed by drying and immersion in 1-MeIM solution	30 minutes+12 hours+12 hours	[30]
9.	ZIF-67	Electrodeposition	$Co(NO_3)_2 \cdot 6H_2O$ (0.145 mol/L)	2-MeIm (0.145 mol/L)	methanol/water solution (10:1 in volume)	Stainless steel mesh was used as the WE and two graphitic plates as counter electrodes (separated by 2 cm) V= -15.0 V	30 minutes	[31]
10.	***ZIF-67***	***Electrodeposition***	***$Co(NO_3)_2 \cdot 6H_2O$ (0.5 Mm)***	***2-MeIm (0.75 mol/L)***	***DMF solution (10 ml)***	***GCE directly electrodeposited with ZIF-67 with Pt wire CE. V= -1.4 V***	***600 seconds***	***Our work***

3.2. Physical Characterization of the developed 3D stacked MOF sensing probe

Physical characterization tools such as SEM, EDX-mapping and XPS analysis were used to initially confirm the formation of the MOFs and their successful stacking over the probe surface.

3.2.1. SEM and EDX Analysis

SEM is a powerful tool to initially deduce the surface morphology of the formed nanostructures over the surface of the probe. A cleaned electrode surface was deposited with the stacked Ni-MOF and Co-MOFs one over the other, with the deposition parameters same as discussed in the preceding section**. Figure 4.3A, B, C** shows the SEM micrograph of the electrode/Ni-MOF/Co-MOF at were various degree of magnifications. **Figure 4.3A-inset** shows only Ni-MOF grown over the electrode surface. Dense structures were seen closely packed on the surface of the electrode stating the parameters of deposition apt for formation of Ni-MOF and Co-MOFs. To understand the distinct morphology of the Co-MOFs, a separate deposition of only the Co-MOFs on a clean electrode was examined. The electrode/Co-MOF was found with distinct cuboidal morphology[32] (orange encircled structure in **Figure 4.3D**) formed on the electrode, magnified Co-MOF morphology shown in **Figure 4.3D (inset i & ii)**. Some spaces on the electrode surface also exhibited clusters of Co-MOFs, as shown in **Figure 4.3E**. The curve shown in **Figure 4.3E** exhibits the normalized particle size distribution curve plotted for a wide area, stating most Co-MOFs to be present between 300 to 400 nm in size range. Hence, the SEM analysis confirmed the uniform deposition of both MOFs onto the surface of the electrode as well as the morphology of Co-MOF deposited through such simple electrodeposition approach for the first time.

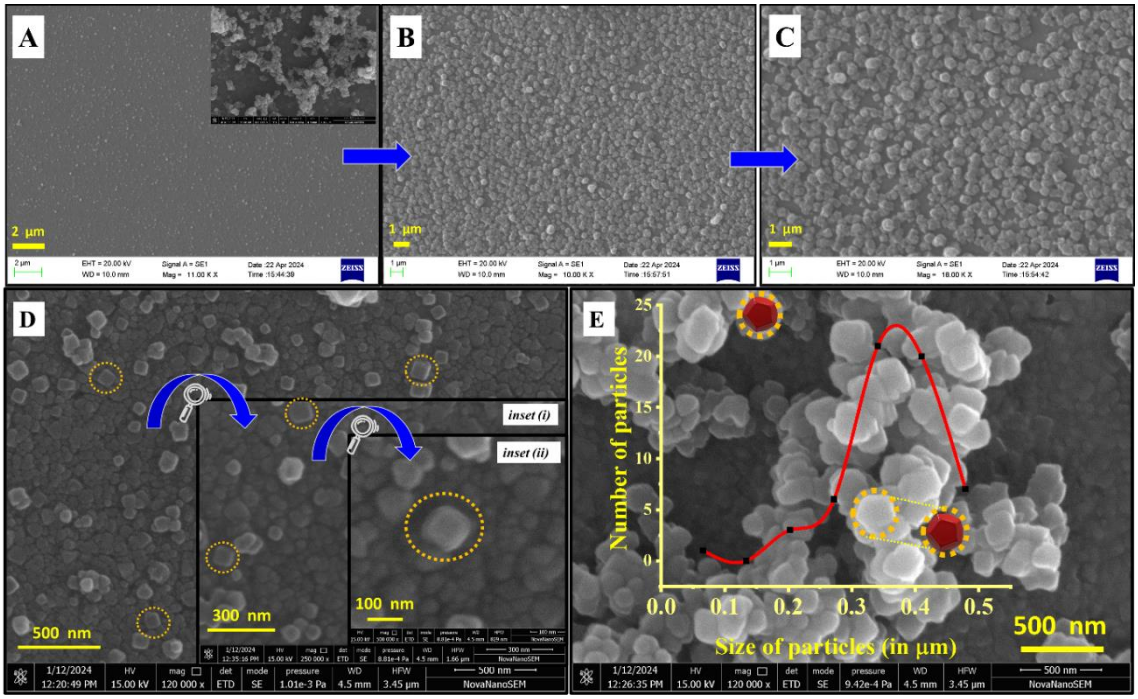

Figure 4.3. ***(A), (B)*** *and* ***(C)*** *SEM micrographs of electrode/Ni-MOF/Co-MOF at varying magnifications;* ***(A-inset)*** *is the SEM micrograph for only Ni-MOF synthesized through the electrochemical route;* ***(D)*** *Co-MOF at varying magnifications* ***(inset i,ii)****;* ***(inset-ii)*** *shows single crystal of Co-MOF encircled in orange dotted line* ***(E)*** *clusters of Co-MOF formed on the electrode surface. The red background curve shows the normal size distribution obtained from SEM images using Image J software. On analysis, the average particle size was found to be between 300 to 400 nm.*

To further deduce the elemental composition of the stacked MOFs and final probe, EDX-elemental mapping of electrode/Ni-MOF/Co-MOF interface and electrode/Ni-MOF/Co-MOF/AuNP surfaces was done. **Figure 4.4A** shows the EDX elemental composition of the developed sensor matrix comprising the stacked MOFs, with peaks corresponding to both the elements being clearly noticeable in electrode/Ni-MOF/Co-MOF. The atomic percentage composition of individual elements viz. Co is 1.86% and Ni is 0.59% in the case **(Figure 4.4A)** which in the final probe i.e. electrode/Ni-MOF/Co-MOF/AuNP remains comparable with an additional presence of Au due to the introduction of AuNP in the layer **(Figure 4.4B).** The Au component can be clearly concluded due to the introductory 8% rise in its composition within final matrix, confirming the successful fabrication on the electrode. For lucid comparative understanding, elemental composition of the structures has been tabulated in their respective spectra reports as inset tables. This

data has been reconfirmed through the mapping outcomes as shown in **Figure 4.4C**. The individual elemental maps have been clearly shown where **Figure 4.4C-I** is the merged micrograph while **4.4C-II, 4.4C-III, 4.4C-IV, 4.4C-V, 4.4C-VI** micrographs correspond to the Co **(red)**, Ni **(green)**, C **(white)**, N **(yellow)** and O **(magenta)** matrix constituents, respectively. The mapping results for only Co-MOF have been shown in **Figure 4.5**.

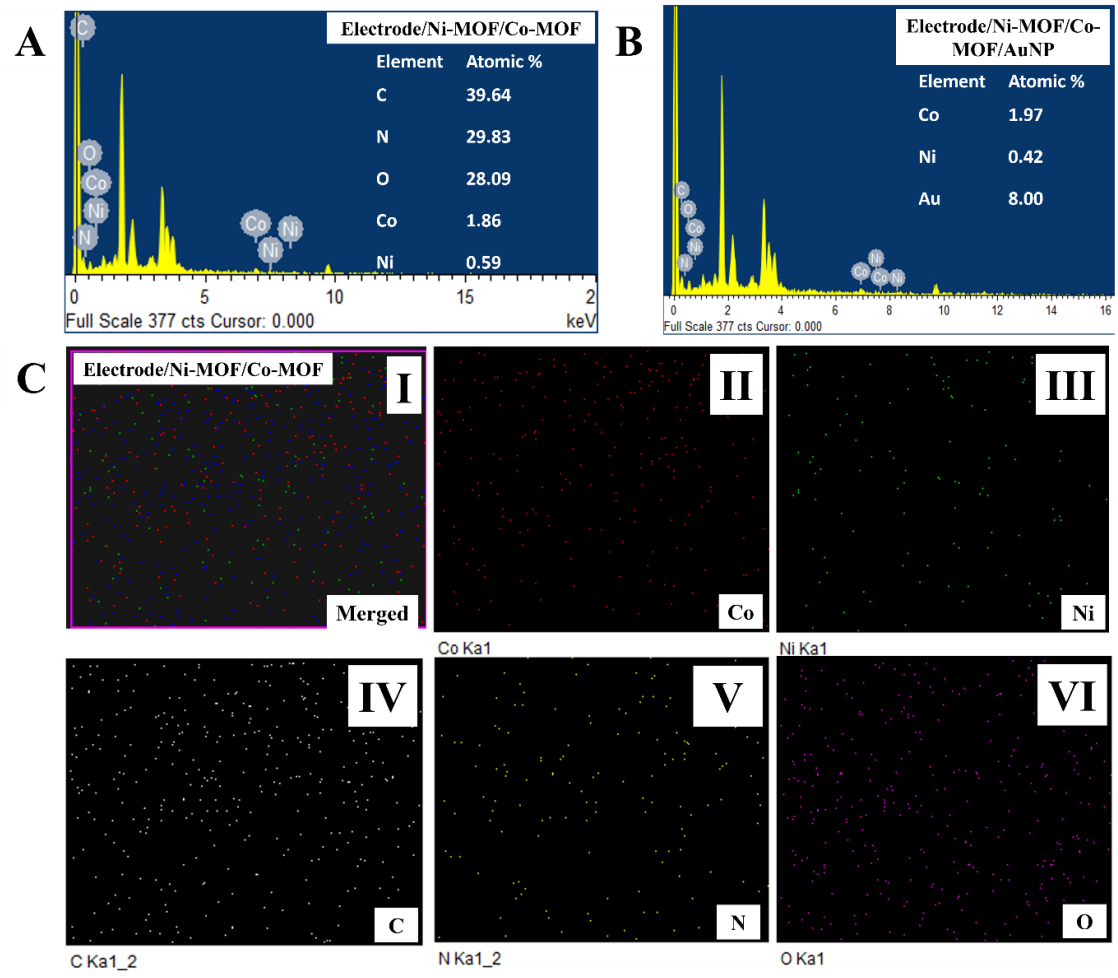

Figure 4.4. ***(A)*** *and* ***(B)*** *are EDX analysis corresponding to electrode/Ni-MOF/Co-MOF interface and electrode/Ni-MOF/Co-MOF/AuNP surfaces, respectively and* ***(C)*** *is the EDX-mapping results corresponding to the individual elements present in an area comprising of Ni-MOF/Co-MOF interfacial surface where,* ***C(I)*** *is the merged micrograph corresponding to electrode/Ni-MOF/Co-MOF;* ***C(II) red*** *coloured micrograph for Co;* ***C(III) green*** *coloured micrograph for Ni;* ***C(IV) white*** *coloured micrograph corresponding to C;* ***C(V) yellow*** *micrograph for N; and* ***C(VI) magenta*** *coloured micrograph corresponding to O.* ***Note:*** *To increase visualization of O micrograph, the colour coding in its individual graph has been changed to magenta.*

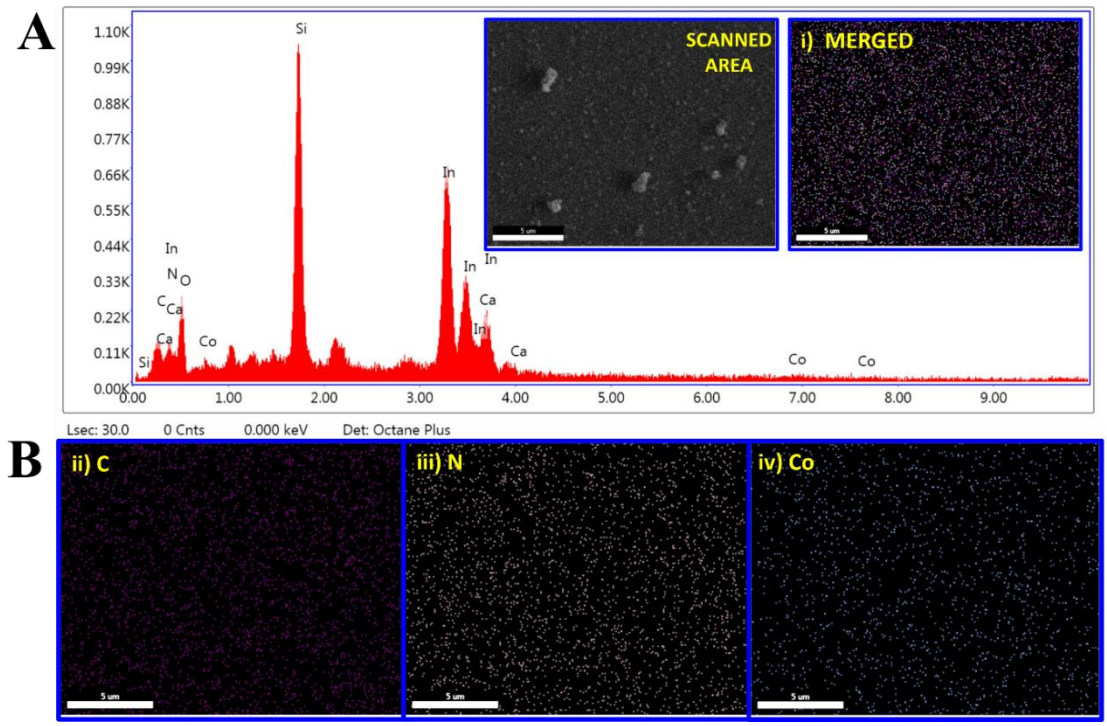

Figure 4.5. *Mapping results for only the Co-MOF layer, where (A) is the EDX spectra for constituting elements in the matrix. Note: the presence of In, Ca and Si in the spectrum is due to the glass coated with ITO used for the MOF fabrication. (B) (i) is the merged micrograph for all MOF elements; (ii) C/carbon elemental micrograph represented in purple color (iii) N/nitrogen elemental mapping results represented in light blue color; and (iv) Co/cobalt micrograph represented in yellow color*

3.2.2. XPS Analysis

To further validate the elemental composition and elucidate the metal oxidation states on the fabricated surface, the probe underwent XPS examination. XPS spectra stating the presence of C1s, N1s, Ni 2p3, Co 2p3, and Au 4f, in stacked MOFs layered with colloidal AuNP within electrode/Ni-MOF/Co-MOF/AuNP are depicted in **Figure 4.6**. The XPS spectra of the bare electrode **(Figure 4.6A)** clearly states the absence of all elements of interest, which on the deposition of the first layer of Ni-MOF brings noticeable changes. The appearance of the C 1s peak due to the presence of the C=C and C-N **(Figure 4.6B-I)** was also further complimented by the presence of N 1s spectrum with a distinct peak at binding energy (B.E). value of 398.38 e.V. **(Figure 4.6B-II)** due to their presence in the MOF backbone, as part of the linker molecule[33,34]. **Figure 4.6B** also demarcates the appearance of the 4 distinct peaks for Ni 2p3 **(Figure 4.6B-III).** While its two peaks are

at a B.E of 855 and 874.4 e.V. which correspond to the $Ni^{2+}(2p_{3/2})$ and $Ni^{2+}(2p_{1/2})$ peaks respectively, the adjoining ones at 860 and 879.4 e.V. correspond to their respective satellite peaks[34,35]. It is important to observe that the comparative analysis in bare electrode surface yields no peaks in the same region, stating them to be purely related to Ni^{2+} metal center in a successfully deposited Ni-MOFs. The intense peaks corresponding to $Ni^{2+}(2p_{3/2})$ and $Ni^{2+}(2p_{1/2})$ establish the presence of Ni core levels in its Ni^{+2} state within the MOF when bonded to imidazole linker moiety. The difference between the core level Ni peaks (19.4 e.V.) and the satellite peaks (19.4 e.V.) remained comparable[35,36]. There are clearly no peaks corresponding to Co and Au due to their absence in the matrix at the current stage **(Figure 4.6B IV, V)**. The C 1s and N 1s peaks remain the same in the 3rd layer **(Figure 4.6C)** too due to their obvious presence in the framework by virtue of the linker moiety (refer **Figure 4.6C I, II)**. On further examination of the XPS spectra for the advancing layers, the preceding elements (**Figure 4.6C I, II, III**) were accompanied with 4 sharp peaks at 780, 784.8, 796.3, and 802.2 e.V. where, the first and third B.E. values corresponded to the $Co^{2+}(2p_{3/2})$ and $Co^{2+}(2p_{1/2})$ peaks while the other two were the adjoining satellite peaks **(Figure 4.6C-IV)**[37,38]. It is to note again that the negative control for the same at the previous electrode surfaces yielded no peaks at the same B.E. values which confirmed the notion for peak generation only due to successful Co-MOF synthesis on the surface[38]. On scanning for the final electrode surface viz., electrode/Ni-MOF/Co-MOF/AuNP, Au 4f reveals two representative doublet peaks at 83.66 and 87.48 e.V. on deconvolution which corresponds to characteristic peaks of metallic Au^0 on its surface due to coating with the colloidal gold particles[39] **(Figure 4.6D-V)**. These peaks are present in only the final surface while being absent in the previous ones **(Figure 4.6 A,B,C-V)** lucidly indicating them, being gold NP originated ones. It is interesting to observe that on subsequent layering of electrode/Ni-MOF with Co-MOF and AuNP, the intensity of the

Ni 2p3 peaks decreases also suggesting proper layering of the succeeding surfaces over it. The XPS analysis, thus, evidenced the presence of both metals as well as non-metals in their desired states on the nanoimprinted surface.

The study re-affirmed us on the successful deposition of the matrix components onto the electrode surface which was further verified through the electrochemical elemental verification, as discussed in the upcoming section.

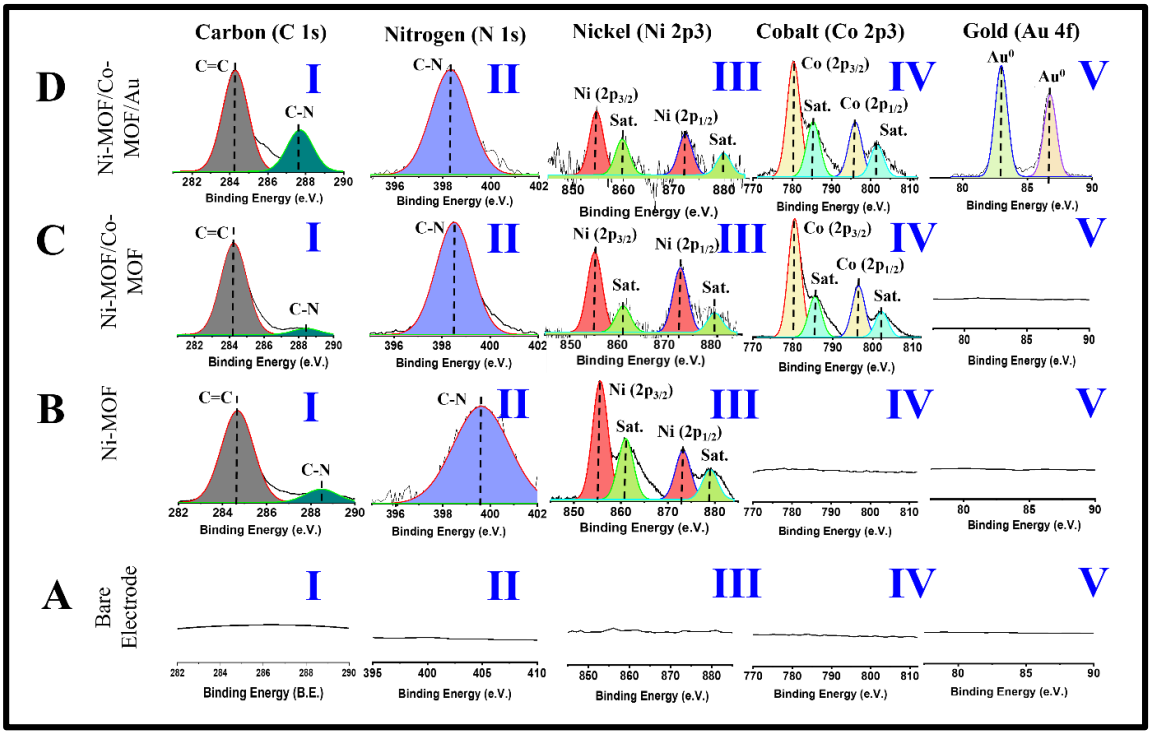

Figure 4.6. *XPS analysis of the* ***(A) Bare electrode*** *surface;* ***(B) Electrode/Ni-MOF****;* ***(C) Electrode/Ni-MOF/Co-MOF;*** *and the final electrode surface* ***(D) Electrode/Ni-MOF/Co-MOF/AuNP*** *in comparison with all preceding probe layers. On stacking the MOFs and coating it with colloidal AuNP, both metal peaks are retained with an additional appearance of peak pertaining to* Au^0.

3.3. Electrochemical characterization

3.3.1. Catalytic metal elemental validation on the GCE/Ni-MOF/Co-MOF/AuNP sensor probe

Following physical characterization investigations that verified the presence of gold metal in the NPs and the metal core of stacked MOFs, electrochemical characterization experiments were conducted to further validate the metal element. Three separate set of

experiments were performed using different electrolytic solutions to validate the presence of Co, Ni and Au metal centers in the composite matrix fabricated. In the very first step, Ni and Co metal centers were determined step-by-step, through electrodeposition of the nanostructures followed by dipping the modified probe into 0.1 M NaOH solution and scanning between -0.4 V vs. Ag/AgCl to +0.5 V vs. Ag/AgCl in case of Ni-MOF **(Figure 4.7A)** and -0.4 V vs. Ag/AgCl to +0.4 V vs. Ag/AgCl, in the case of Co-MOF **(Figure 4.7B)**. On deposition and scanning the probe for testing of 'Ni' metal center at the primary stage, the characteristic redox peaks pertaining to Ni^{2+} were observed at +0.32 V vs. Ag/AgCl and -0.33 V vs. Ag/AgCl. Comparable redox potentials values for Ni^{2+} have been reported in previous articles too, with similar profiling solvent, validating the desirable state of Ni[22]. On further modification of the GCE/Ni-MOF probe by stacking it with Co-MOF, along with the previous noted peaks for Ni redox, an additional enhanced peak at +0.32 V for Co^{+2} was also observed in the oxidation window, whereas, the reduction peak intensity at -0.33 V was further enhanced in magnitude due to the superimposing of the reduction peak for both the metals at the same potential[40,41]. Additionally, a similar set of experiment was performed to determine the presence of 'Au' metal in the top coat of final probe comprising colloidal AuNP **(Figure 4.7C)**. As anticipated, a redox peak at around +1.2 V vs. Ag/AgCl and +1.05 V vs. Ag/AgCl was seen when dipping the electrode in 0.5 M H_2SO_4 scanned within a potential window of +0.8 V vs. Ag/AgCl to +1.4 V vs. Ag/AgCl[42]. A control experiment where the unmodified probe was dipped in the same electrolytic solutions within the same potential range was performed, which yielded no results. The stability of the individual probe layers and electron transfer mechanisms were validated through a scan rate study as well. The anodic (Ipa) and cathodic (Ipc) peak currents were found directly proportional to the scan rates, with the correlation coefficient values of 0.99 and 0.97 for 'Ni' in Ni-MOF (**inset Figure**

4.7A), 0.99 and 0.98 for 'Co' in Co-MOFs (**inset Figure 4.7B)**, and 0.99 and 0.99 for 'Au' in AuNP **(Figure 4.7D)**, respectively. This demonstrates the stable surface adsorption/adhesion phenomena with stability even at higher scan rates, making the engineered probe ideal for sensing applications. Thus, the set of physical and electrochemical characterization studies conclusively validated the presence, composition and overall morphology of the constituting metallic nanostructures in the final GCE/Ni-MOF/Co-MOF/AuNP sensing probe.

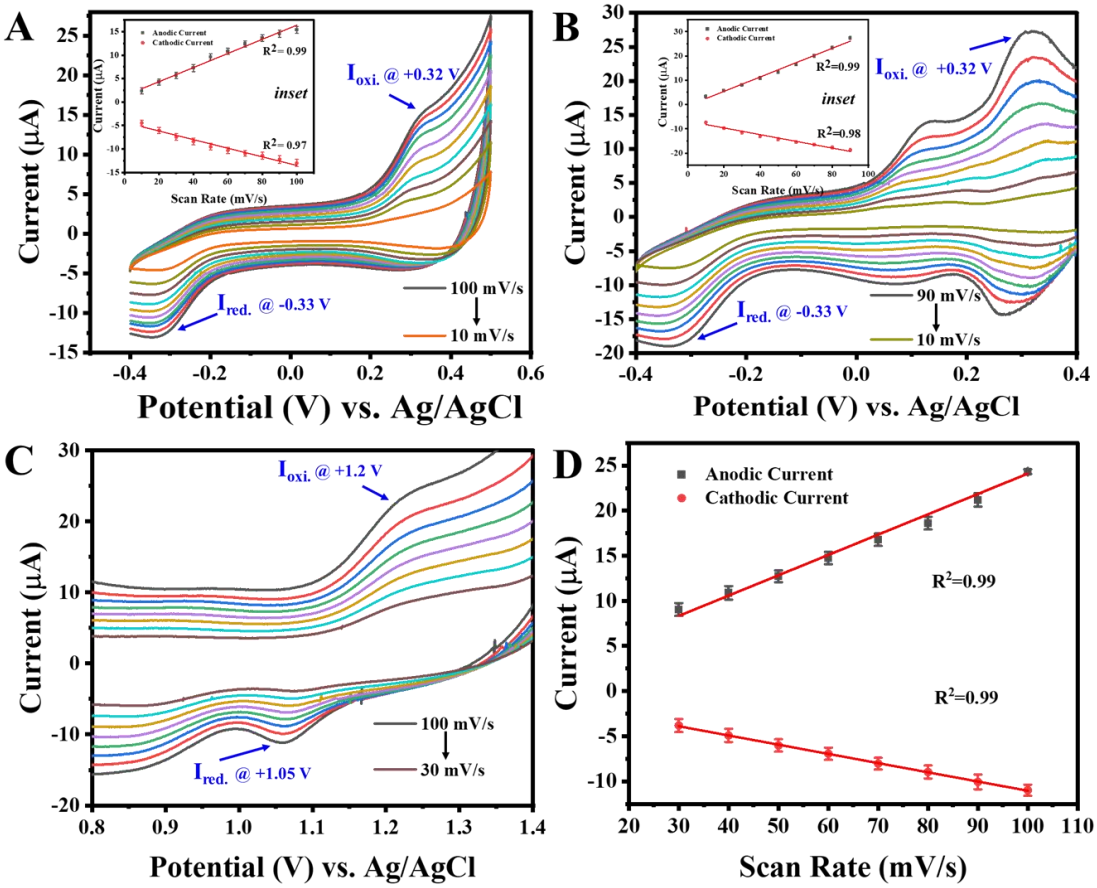

Figure 4.7. *Electrochemical estimation of probe elements where* ***(A)*** *is the CV curve corresponding to redox behaviour of Ni-MOF in the presence of 0.1 M NaOH at different scan rates ranging from 10-100 mV/s (n=5),* ***inset*** *depicts the corresponding fitting curve for the redox values;* ***(B)*** *is the CV curve corresponding to redox behaviour of Co-MOF in the presence of 0.1 M NaOH at different scan rates ranging from 10-90 mV/s (n=5),* ***inset*** *shows the corresponding fitting curve for the redox values.* ***(C)*** *is the CV curve corresponding to redox behaviour of colloidal AuNP in the presence of 0.5 M H_2SO_4 at different scan rates ranging from 30-100 mV/s (n=5), and* ***(D)*** *is its corresponding fitting curve.*

3.3.2. Electrochemical performance of the stacked MOFs in the sensor probe

After confirmation of the desirable metals on the surface of the developed matrix, electrochemical examination was conducted to understand it's charge transfer behaviour and electrocatalytic capabilities. The electrochemical examination of the developed surface was done through dipping the probe in ZS and scanning it at a scan rate of 50 mV/s (n=5) at room temperature within a potential window of -0.15 V vs. Ag/AgCl to +0.75 V vs. Ag/AgCl. Sharp redox peaks were observed for all surfaces within the potential range for the (K_3[Fe (CN)$_6$]/K_4[Fe (CN)$_6$]) redox species. Redox peaks were observed at +0.45 V vs. Ag/AgCl and +0.065 V vs. Ag/AgCl in correspondence to the intrinsic behaviour of ZS at the bare GCE surface **(black curve)**. A significant shift at a lower potential and higher current magnitude in the peak was observed for the same ZS species at +0.25 V vs. Ag/AgCl and +0.20 V vs. Ag/AgCl for GCE/Ni-MOF **(red curve)**. Similar enhanced peaks at the lower potential and higher current magnitude pertaining to GCE/Co-MOF **(blue curve)** and GCE/Ni-MOF/Co-MOF **(green curve)**, were further obtained on consecutive fabrication steps, as shown in **Figure 4.8A** (n=5). The lower potential shift and higher current magnitude cumulatively demarcate the layer's catalytic as well as charge transfer characteristics. Comparative histograms depict the cathodic and anodic responses of the electrode surfaces on successive modifications **(Figure 4.8A-inset).** The modified surface, i.e., GCE/Ni-MOF/Co-MOF comprising of the stacked MOFs exhibited the highest charge transfer characteristics and electrocatalytic behaviour when compared to the individual surfaces with the single metal MOFs. The proficiency of the stacked MOFs to conduct the electrons more efficiently can be attributed to the conductive metal synergies facilitating seamless electron transfer[43]. The charge transfer characteristics of individual surfaces could be a function of their respective surface areas on the electrode, as calculated through the below **Randles Sevcik equation**[44] **(equation i)**,

$$I_p = \left(2.69\times10^5\right) n^{3/2}\, ACD^{1/2}\, v^{1/2} \quad \text{..... Equation i}$$

where, surface area of the electrode is denoted by ***A*** *(in* ***cm^2****), the anodic peak current is depicted through* ***I$_p$*** *in terms of ampere,* ***v*** *is the scan rate in* ***V s^{-1}****, the number of electrons transferred in the redox process are represented by* ***n****, concentration of the transferred redox species is stated by* ***C in mol cm^{-3}****, and the diffusion coefficient is denoted by* ***D*** *which is in* ***cm^2 s^{-1}****.*

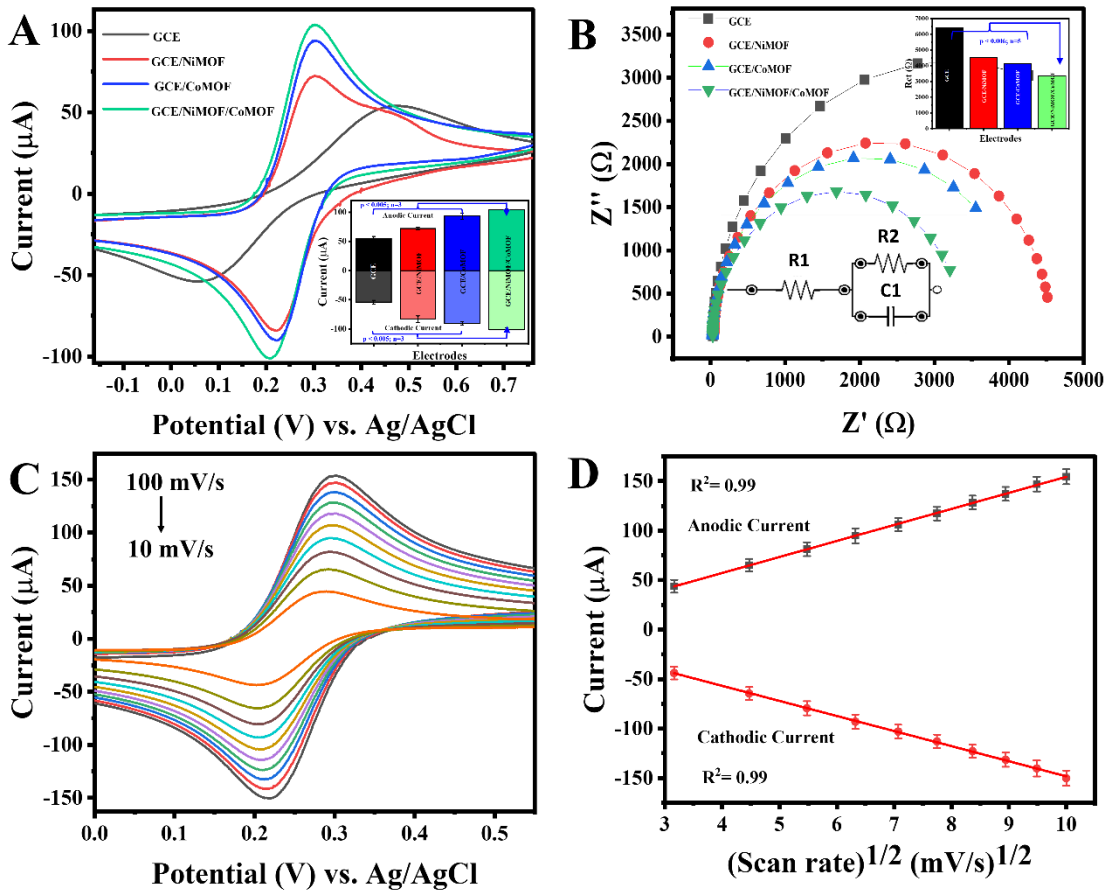

Figure 4.8. ***(A)*** *CV response of bare GCE* ***(black curve)****, GCE/Ni-MOF* ***(red curve)****, GCE/Co-MOF* ***(blue curve),*** *and GCE/Ni-MOF/Co-MOF* ***(green curve)*** *in ZS (5 mM; pH-7, scan rate- 50 mV/s; n=5);* ***inset*** *depicts comparative histogram of the anodic and cathodic current responses corresponding to each surface, with an amplified response for the GCE/Ni-MOF/Co-MOF electrode.* ***(B)*** *EIS response in the form of Nyquist plots for bare GCE* ***(black curve)****, GCE/Ni-MOF* ***(red curve)****, GCE/Co-MOF* ***(blue curve),*** *and GCE/Ni-MOF/Co-MOF* ***(green curve)*** *in ZS (5 mM; pH-7; n=5) with its equivalent circuit model where* ***R1*** *denotes the solution resistance,* ***R2*** *denotes the charge transfer resistance (Rct), and* ***C1*** *is the double layer capacitance;* ***inset*** *shows a comparative histogram displays the Rct values of each surface.* ***(C)*** *Scan rate study of GCE/Ni-MOF/Co-MOF in ZS solution at varying scan rates ranging between 10-100 mV/s;* ***(D)*** *obtained linear plot corresponding to current vs. (scan rate)$^{1/2}$.*

The calculated effective surface area of each surface, viz., GCE, GCE/Ni-MOF, GCE/Co-MOF, GCE/Ni-MOF/Co-MOF was 66.6×10^{-3} cm^2, 89.27×10^{-3} cm^2, 116.13×10^{-3} cm^2, and 127.95×10^{-3} cm^2, respectively. These results are in agreement to our electro-characterization results that the electrocatalytic potential of the layers increase with successive layering of the matrix with individual MOFs and is maximum in case of the stacked MOFs. The area of the GCE/Ni-MOF/Co-MOF increases by 1.92, 1.43, and 1.10 times when compared to bare GCE, GCE/Ni-MOF, and GCE/Co-MOF, respectively. The CV results were further validated using the EIS study **(Figure 4.8B).** Upon fitting the obtained values to the Randles circuit the Nyquist plots were determined for the respective surfaces. Briefly, the Randles circuit is an equivalent electrical circuit which comprises of a resistance (R1), which actually is a resistance of the solution, coupled in series with double layer capacitance (C1) and faradaic charge transfer resistance (Rct/R2) connected to each other in parallel. The Rct/R2 calculated through the Nyquist plots were 6393 ± 4.55 Ω, 4509 ± 1.33 Ω, 4154 ± 7.54 Ω, and 3364 ± 2.7 Ω, respectively for bare GCE **(black curve)**, GCE/Ni-MOF **(red curve)**, GCE/Co-MOF **(blue curve)**, and GCE/Ni-MOF/Co-MOF **(green curve)** electrodes, respectively. The results of the EIS study verify the outcomes of the CV results indicating that the GCE/Ni-MOF/Co-MOF has the lowest resistance and therefore the greatest charge transfer characteristics **(Figure 4.8B-inset)**. Hence, it can now be checked for its catalytic potential against the target analyte for establishing it as a sensing platform. In the meantime, the robustness of the platform was also assessed using a small yet crucial control experiment, where the developed probe was scanned at varying scan rates (from 100 mV s^{-1} to 10 mV s^{-1}) within a potential window of 0.0 V vs. Ag/AgCl to +0.5 V vs. Ag/AgCl in the same electrolytic solution (5mM ZS). The peak oxidative and reductive currents (I_{pa} and I_{pc}) were found to be proportionate to the square root of the scan rates with a correlation coefficient of 0.99 in

both the cases evoking the exceptional stability of the probe even at higher and lower scan rates in a diffusion-controlled manner, as shown in **Figure 4.8C and 4.8D**. The electrochemical investigations so far state the potential usability of the sensor probe for forthcoming applications.

3.4. Analytical Feasibility of the Developed Surface

To check the feasibility of the developed system, NO_2^- was used as the target analyte, whose detection importance has been stated through an elaborate discussion made in the introductory section. On thorough survey of the developed sensors against NO_2^-, it was understood that the Au core particles engage optimally to form a stable Au-N bond with 'N' of the nitrite anions along with providing a huge surface area for NO_2^- adhesion[4,17,45–47]. To reap benefit of this established notion, we introduced a layer of colloidal AuNP onto the matrix aiding towards increased sensing efficiency of the developed surface, making the final surface as GCE/Ni-MOF/Co-MOF/AuNP. This developed system was subjected to rigorous testing against the analyte where preliminary testing involved control studies. At first, each electrode surface was tested against NO_2^- to ascertain the contribution of each metallic architecture. LSV was performed for the bare GCE within a range of +0.5 V vs. Ag/AgCl to +1.0 V vs. Ag/AgCl in a 0.1 M PBS solution containing 0.1 M NO_2^- (n=3). A slight oxidative current was recorded at approximately +1.0 V vs. Ag/AgCl with no distinct peaks in the scanned window (**Figure 4.9A, black curve**) since unmodified bare electrodes are known to detect NO_2^- but suffer from large overpotential, demanding suitable electrode modifications for their commercial sensing utility[13]. A clear shift in the peaks towards the lower potential with improved current magnitude was seen on subsequent surface modifications, proving the catalytic ability of the modified surfaces against NO_2^- with a distinct peak at +0.95 V vs. Ag/AgCl. The anodic peak was constantly enhanced on addition of each consecutive layer one over the other, investigated in similar

experimental conditions **(Figure 4.9A)**. Because of the Ni-Co synergy and the interaction between Au and the analyte species, the final layer showed the highest current value in the presence of the analyte. When compared to the unaltered bare GCE surface, there was approximately 4.83-fold increase in signal responsiveness against the oxidative irreversible conversion of NO_2^- to nitrates. A comparative histogram was plotted to understand the quantitative rise in signal output **(Figure 4.9B)**, pictorially stating the same. To eliminate the possibility of signal interference by PBS, the bare GCE probe was subjected to pristine PBS solution, yet yielded no response **(olive curve, Figure 4.9A)**.

To further validate that the signal outcomes were a result of the target analyte only, a set of control experiments were performed. The first control test was meant to understand the response of the GCE/Ni-MOF/Co-MOF/AuNP probe against the target analyte. For the test, relatively higher concentrations of NO_2^- solutions (0.1 M to 0.5 M) in 0.1 M PBS were prepared and tested against GCE/Ni-MOF/Co-MOF/AuNP via LSV **(Figure 4.9C)**. A linear trend was obtained in the standard plot with gradual increase in the concentrations of NO_2^- with a correlation coefficient of 0.97 **(Figure 4.9D)**. The obtained regression equation can be stated as,

$$\Delta I\ (\mu A) = (1248.64 \pm 226.63) + 12179\ (\pm 931.72) \times \text{Conc.}\ [NO_2^-\ (M)].$$

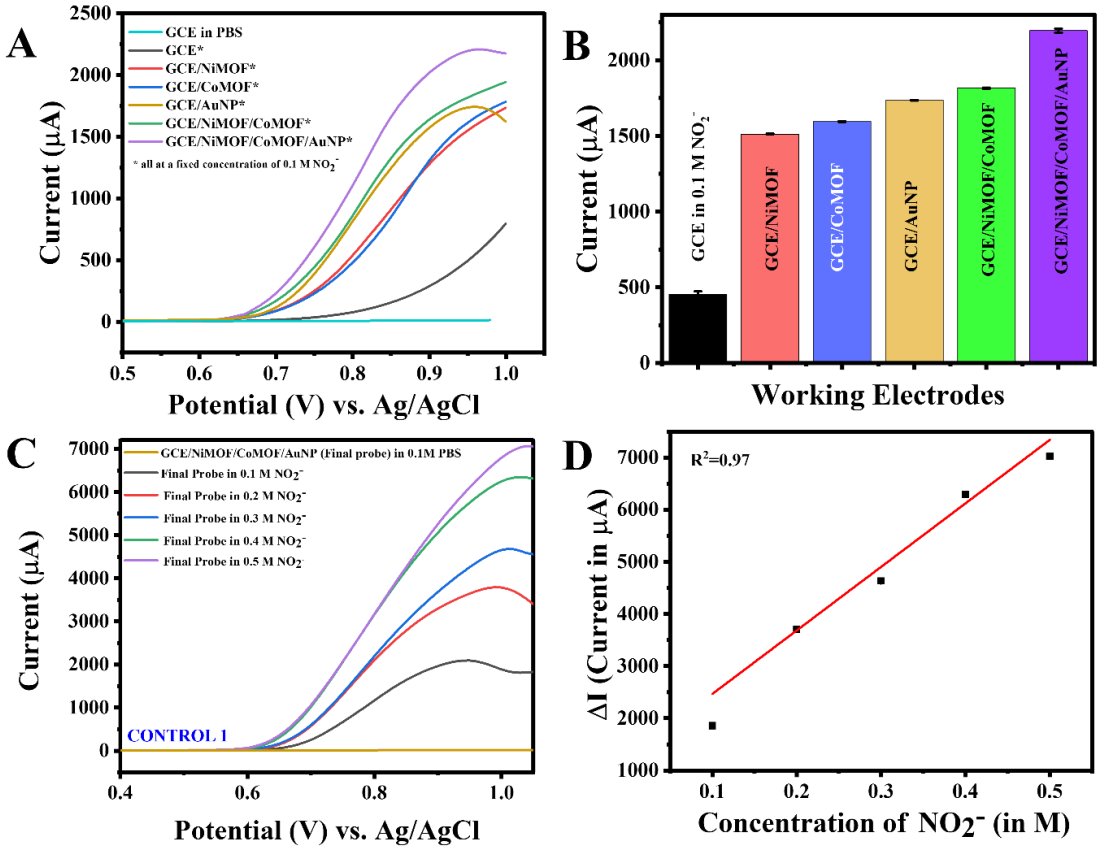

Figure 4.9 ***(A)*** *Layer by layer analysis of the sensor matrix components against the target analyte, i.e. 0.1 M* NO_2^-. ***(B)*** *Comparative histogram for the analysis* ***(C)*** *Concentration dependent analysis of the final probe, i.e. GCE/Ni-MOF/Co-MOF/AuNP against higher concentrations of the analyte* ***(D)*** *Corresponding linear regression plot for the probe against the concentrations.*

Another control study, i.e. the scan-rate dependent study was conducted in the presence of 0.1 M NO_2^-. The experiment comprised of ranging the scan rates from 10 mV/s to 100 mV/s in 0.1 M NO_2^- solution, where a rise in anodic current response was recorded with an increase in square root of the scan rate (n=3) with a correlation coefficient of 0.98 (**Figure 4.10, Figure 4.10-inset**). Both the control experiments conclusively proved the robustness, stability and direct sensing capabilities of the platform for NO_2^-

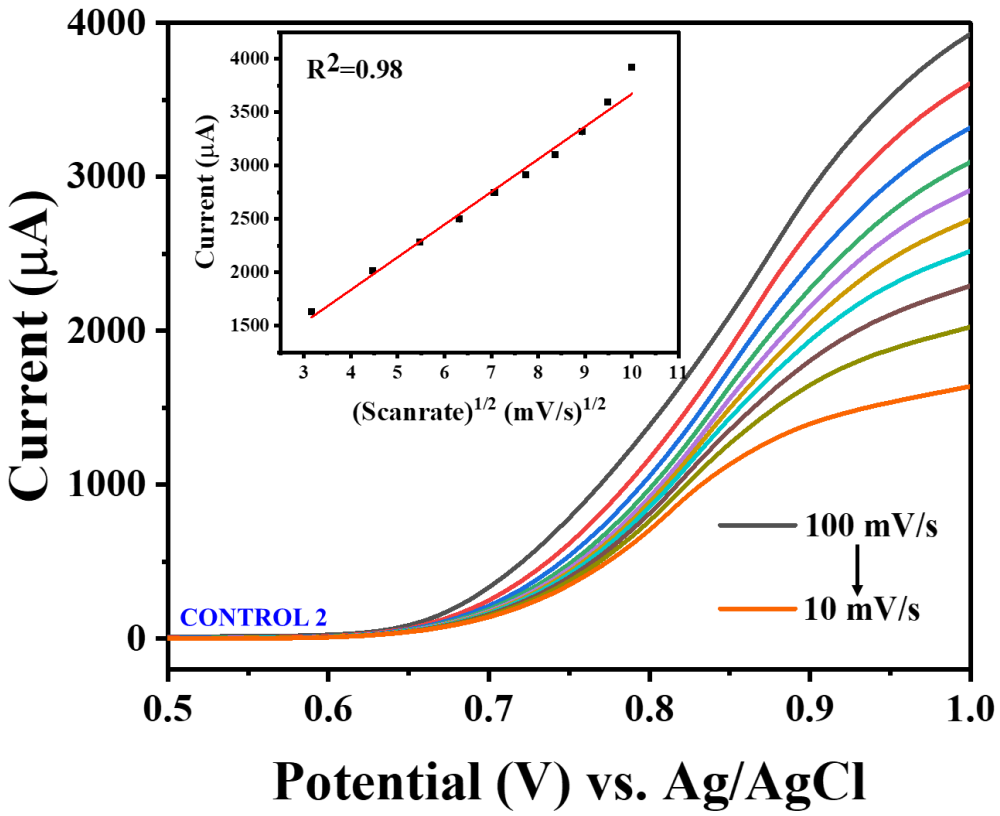

Figure 4.10. *Scan rate study of the final probe in 0.1 M NO_2^-, inset depicting the anodic current verses square root of scan rate.*

The analytical abilities of the GCE/Ni-MOF/Co-MOF/AuNP was further examined by deployment of chronoamperometry (**Figure 4.11A**). At first, the response of the final probe was recorded at +1.0 V vs. Ag/AgCl in PBS (**blank red curve**). Further the interface was investigated against a dose-dependent study of NO_2^- at the same potential and the signal response was noted. With rise in the concentration of NO_2^-, the shift from the blank reading was widened, generating a noticeable 'ΔI' in each case. Two linear calibration plots were obtained in the dosage range, one from 0.01 to 10 µM (R^2=0.91) and the other from 100 to 1000 µM (R^2=0.97), covering an overall wide linear range from 0.01 to 1000 µM, having a detection limit (LOD) of 4.2 nM, as suggestive by the chronoamperometric data (**Figure 4.11B**). Appearance of such ranges can be attributed to the differential saturation of analyte onto the electrode surface with rapid interaction at the lower concentrations, generating steeper slope[48]. The LOD was calculated using the **equation ii** which is

$$LOD = \frac{3\sigma_b}{m} \qquad \textbf{……Equation ii}$$

where σ_b represents the blank sample's standard deviation, and m is the calibration plot's slope

The regression equations for the lower and higher concentrations ranges were obtained from the standard curves, represented as follows:

Regression equation 1: (0.01 to 10 µM)

I (µA) = 0.688 (±0.09) + 0.071 (±0.015) x [Conc. of NO_2^- (µM)].

Regression equation 2: (100 to 1000 µM)

I (µA) = 1.096 (±0.234) + 0.00623 (±4.16) x. [Conc. of NO_2^- (µM)].

3.5. Response Time Analysis for the GCE/Ni-MOF/Co-MOF/AuNP Sensor

Response time, a crucial parameter in sensor performance analysis is defined by the time needed for the sensing interface to generate a signal response after the analyte is spiked. For determining the same in case of our platform, a chronoamperometric run was performed by dipping the sensing probe in 0.1 M PBS to obtain a stable signal **(Figure 4.11C, point a)**. Following which, a known concentration of NO_2^- was injected into the electrolytic solution **(point b)**. Interestingly, a sharp rise in the current **(point c)** was observed between 317.20 seconds and 318 seconds, followed by observance of a current saturation point **(point d)**. The signal was obtained at +1.0 V (same as the calibration study in previous section) and the response time was found to be 0.80 seconds (318-317.20), highlighting the ultra-swift sensing capability of the platform. **Figure 4.11C** depicts the real-time response generated by testing the sensor against 1000 µM of NO_2^-. We also examined the sensor response against different concentrations of NO_2^-, and the sensor exhibited commendable response with an average response time of <1.5 seconds in all cases.

The developed sensor has been extensively evaluated in terms of various governing parameters and compared to the latest ones in the literature, as represented in **Table 4.2 (at the end of the chapter, as *Chapter Annexure*)**. Most of them either lag behind in covering the permissible limit of WHO, or have tedious steps of fabrication with elongated fabrication period. The engineered surface is highly resilient and beneficial in multiple ways with the biggest advantage being a simple fabrication approach and a rapid detection of NO_2^-, covering the WHO permissible limits and beyond.

3.6. Selectivity, Reproducibility, and Stability of the GCE/Ni-MOF/Co-MOF/AuNP Sensor Probe

Selectivity is one of the most important characteristics that a sensor possesses. For an electrochemical sensor, it is an important trait of it to detect only the target analyte in the effective potential window scanned. To understand the same, a range of possible ions and related compounds were tested against the signal probe. Interferents such as Cl^-, CO_3^{2-}, SO_4^{2-}, H_2PO^{4-}, Sucrose, D-Glucose, Lactate Monohydrate, Sodium Nitrate, L-histidine, L-methionine, K^+ were tested against a possible response generation at a concentration as high as 1 M, but yielded no result at the NO_2^- signature oxidation potential of +1.0 V vs. Ag/AgCl (**Figure 4.11D**). The study proved the efficacy of the sensor selectively to the target analyte.

The coefficient of selectivity (K_{sel}) of the coexisting molecules was determined using **equation iii,** found between 0.026 to 0.119, for which their respective individual values have been stated in **Table 4.3**.

$$K_{sel} = Signal_{interfering\ molecule}/Signal_{NO_2^-} \quad \text{……. } \textbf{\textit{Equation iii}}$$

Table 4.3. *Co-efficient of selectivity for possible interferent species present in the real samples.*

Co-existing molecules	Current (µA)	$K_{sel.}$
Cl^-	0.41	0.050
CO_3^{2-}	0.607	0.074
SO_4^{2-}	0.979	0.119
H_2PO^{4-}	0.336	0.041
Sucrose	0.371	0.045
D-Glucose	0.266	0.032
Lactate Monohydrate	0.255	0.031
Sodium Nitrate	0.371	0.045
L-histidine	0.21	0.026
L-methionine	0.805	0.098
K^+	0.979	0.119
NO_2^-	8.16	1

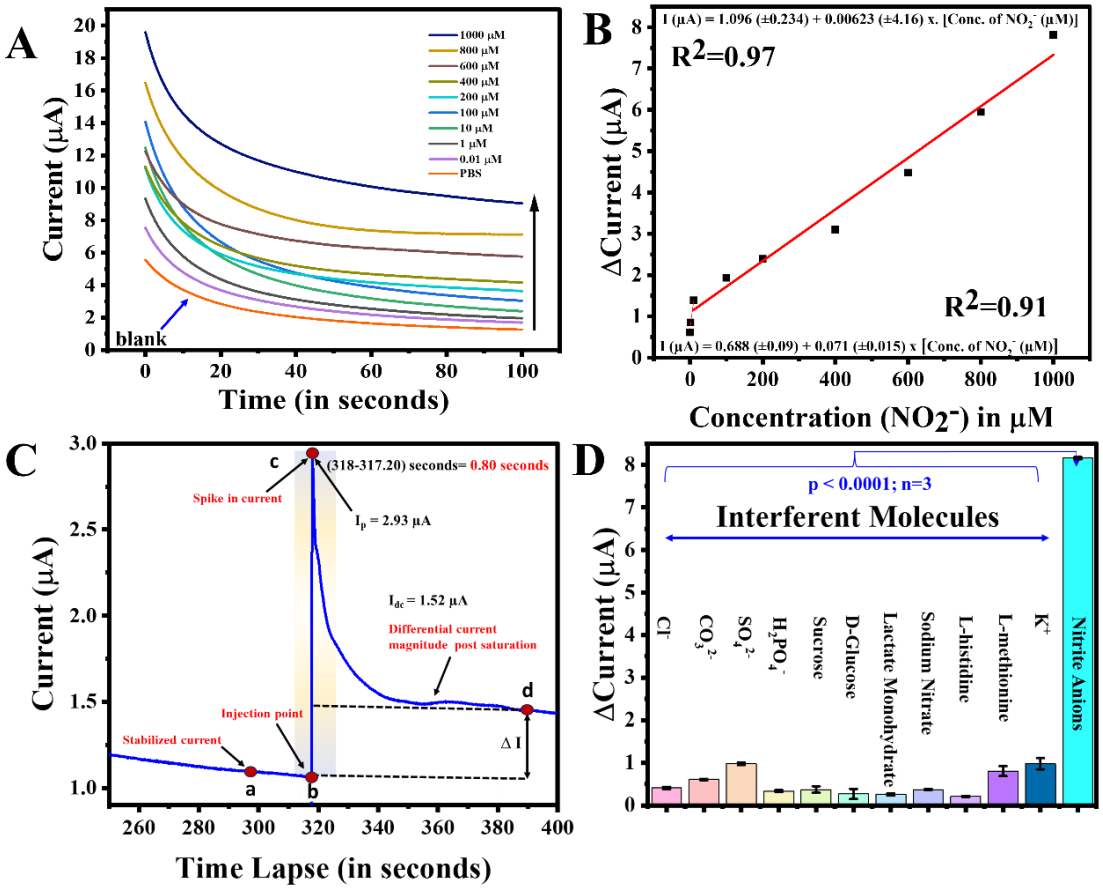

Figure 4.11. ***(A)*** *Dose dependent study for varying concentrations of NO_2^-* ***(B)*** *Calibration plot* ***(C)*** *Response time analysis* ***(D)*** *Interference study of the sensor against a range of possible interferents likely to be present in the real sample premises*

In further course of action, an independent study governing the reproducibility of the response at five different electrodes in a sample solution containing 1000 µM of the target analyte was registered **(Figure 4.12A).** A negligible deviation in the current response was observed across all tested electrodes (RSD 3.7 %, n=3), which can be a function of handling errors or mild changes in testing conditions such as environmental factors.

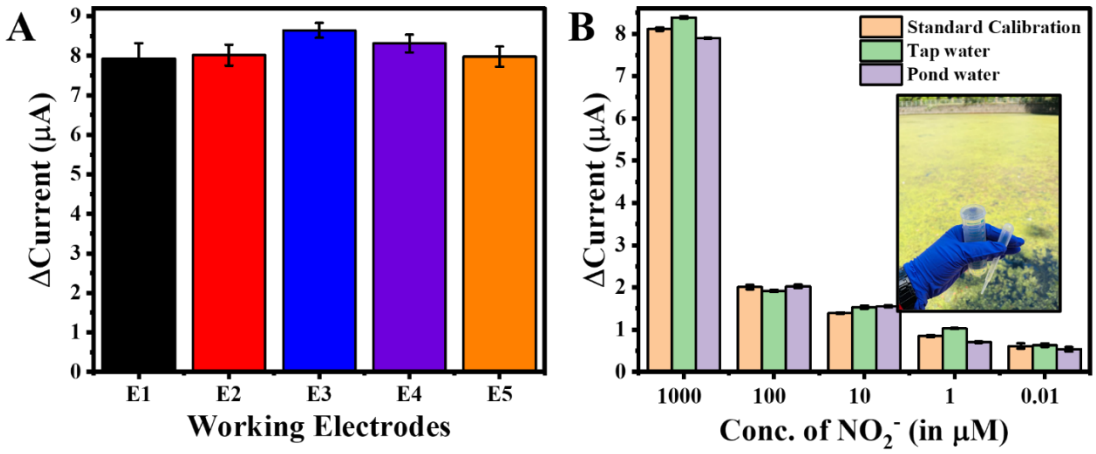

Figure 4.12. ***(A)*** *Probe reproducibility analysis in a range of electrodes.* ***(B)*** *Real sample study of the sensor involving tap water and pond water.*

3.7. Real Sample Analysis

NO_2^- a common fertilizer for plants and a food preservative can often be exploited or misused, cascading generation of carcinogens and result into ill-health[46]. In view of this, the developed sensor was tested for NO_2^- in its natural premises such as tap water and pond water to understand its practical applicability. A standard spike and recovery route was adopted for validating NO_2^- concentrations in spiked real water samples in the concentration range of 0.01 to 1000 µM under optimized experimental settings. Chronoamperometric response was recorded in a dose-dependent manner as a function of NO_2^- in PBS-equilibrated water samples and then compared to the standard calibration plot obtained in **Section 3.4,** as represented through bar graphs in **Figure 4.12B.** The figure depicts the histogram-based analysis of the real samples results adjacent to the standard calibration curve, evoking optimal sensor behaviour even in real-sample matrices. The recoveries were calculated at each tested concentration of NO_2^- using

equation iv, and was found between 95.32 to 108 % in tap water (RSD%= 3.60, n=5) and 93 to 100.89% in pond water, respectively (RSD%= 4.80, n=5).

$$\%\ Recovery = (S_{NO_2^-} - B_{NO_2^-})/(SS_{NO_2^-}) * 100 \quad \ldots\ \textbf{\textit{Equation iv}}$$

where, [S] and [B] are the analytical responses of the GCE/Ni-MOF/Co-MOF/AuNP sensing platform in PBS spiked with real samples and blank PBS, respectively while [SS] correspond to response of the standard buffer with the same concentration of NO_2^-, under consideration.

It is worthy to mention that the designed sensing matrix, i.e., GCE/Ni-MOF/Co-MOF/AuNP, is capable to detect NO_2^- in a wide range, even covering the recommended permissible limits of it (<65 µM) in drinking water and beyond, as per the guidelines of the WHO[45,49]. The discussed findings strongly instigate that the fabricated engineered sensing surface comprising of two stacked MOFs is an interesting and potent platform capable of estimating NO_2^-, revealing its future commercial prospects.

3.8. Integration of Sensor with a Smartphone Interface for Field Deployment

A conventional system utilizes multi-stepped analysis and conclusive comments by an expert on the basis of a generated current response by a CA curve obtained at a specific potential to quantitatively estimate NO_2^- in a setup. To minimize these steps and remove possibility of errors caused by manual interventions, an automated data analysis and display smartphone application **(NitriSens app)** has been developed to create a user-friendly experience. It was a specially designed application for the purpose of quantitative estimation of NO_2^- in water samples. The app was programmed using Flutterflow software assisted by an in-built editor utilizing Dart language. The app development cycle has been briefly stated in **Figure 4.13** (step **1-10**), as a flowchart, involving all crucial steps such as ideation and multi-iterative optimizations.

Figure 4.13. *The '**NitriSens'** software's developmental cycle.*

The NO_2^- app namely, '**NitriSens**', was built over an android platform for developing a hand-held device where the calibration plot had already been fed, allowing real-time information of the NO_2^- value on a given real sample **(Figure 4.14)**. The results are displayed with a caution message, stating the NO_2^- levels in the sample as 'SAFE' or 'UNSAFE', giving a hassle-free and easily understandable response output. The results can also be re-visited by the user in future by referring to the History section of the app post saving the particular entry (steps **(A-E)** briefly demonstrated in **Figure 4.14**). A drive link with all information pertaining to the app including the software code components can be accessed via a link mentioned below.

Google drive link here:

https://drive.google.com/drive/folders/1IRbZeTk1YBU_2Ec4KE16ZiG1n-ZqPriY

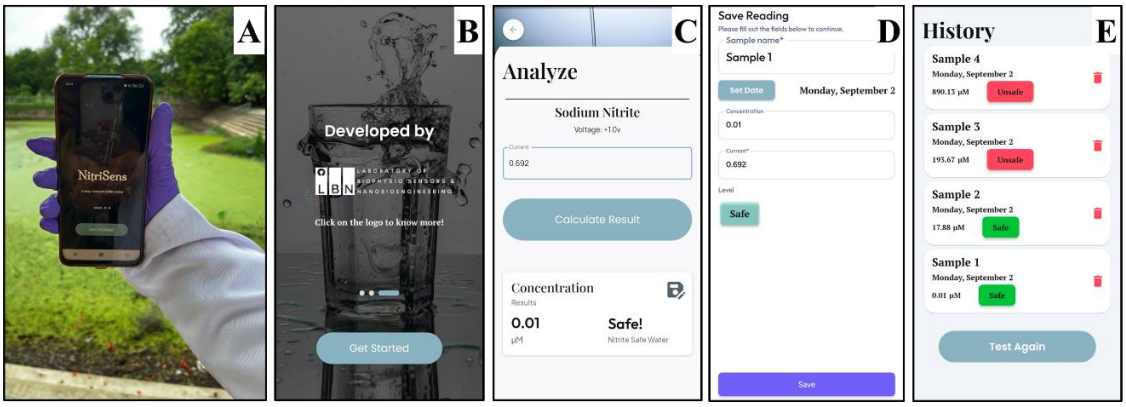

Figure 4.14. *Brief demonstration of the software user-interface.* ***(A)*** *The software user interface (primary page);* ***(B)*** *Brief introduction* ***(C)*** *Analysis window where the current value is to be fed by the user, followed by clicking on '**Calculate result**' button;* ***(D)*** *Display of results in form of quantitative NO_2^- estimation, with clear information about safe/unsafe NO_2^- levels in the test sample;* ***(VI)*** *Saved history of the results obtained, for future reference.*

4. Conclusion

In this study, a novel approach was adopted to fabricate Co-MOF at a low potential in a short fabrication time, as low as 600 seconds. The developed Co-MOF was then assembled as a crucial component within a sensing matrix by stacking over a Ni-MOF surface. The surface was further conjugated with AuNP to engineer the final sensing probe as GCE/Ni-MOF/Co-MOF/AuNP. The sensor probe surface was studied extensively using a plethora of physical and electrochemical characterization methods ranging from SEM-EDX to XPS, followed by electrochemical validation studies. Then, the sensor analytics were established deploying CV, EIS, and chronoamperometry. The developed sensor is interesting attributed to its simple steps of fabrication, a wide LDR and LOD against NO_2^-, a lighting fast response time of <1.5 seconds, and commendable selectivity towards the analyte even in the presence of interfering species. This is the first report of its kind where such a stacked MOF-based platform has been deployed for NO_2^- sensing purpose along with a smartphone interface giving real-time qualitative and quantitative concentration outputs using only current as an input. Such a handheld analytical platform could be a valuable asset for futuristic field-deployable sensing applications for a range of molecules, including NO_2^-, driving human and environmental well-being.

REFERENCES

(1) Parvizishad, M.; Dalvand, A.; Mahvi, A. H.; Goodarzi, F. A Review of Adverse Effects and Benefits of Nitrate and Nitrite in Drinking Water and Food on Human Health. *Heal. Scope* **2017**, *In Press* (In Press). https://doi.org/10.5812/jhealthscope.14164.

(2) Radhakrishnan, S.; Krishnamoorthy, K.; Sekar, C.; Wilson, J.; Kim, S. J. A Highly Sensitive Electrochemical Sensor for Nitrite Detection Based on Fe2O3 Nanoparticles Decorated Reduced Graphene Oxide Nanosheets. *Appl. Catal. B Environ.* **2014**, *148–149*, 22–28. https://doi.org/10.1016/j.apcatb.2013.10.044.

(3) Walters, C. L. The Exposure of Humans to Nitrite. *Oncology* **2009**, *37* (4), 289–296. https://doi.org/10.1159/000225455.

(4) Mo, R.; Wang, X.; Yuan, Q.; Yan, X.; Su, T.; Feng, Y.; Lv, L.; Zhou, C.; Hong, P.; Sun, S.; Wang, Z.; Li, C. Electrochemical Determination of Nitrite by Au Nanoparticle/Graphene-Chitosan Modified Electrode. *Sensors (Switzerland)* **2018**, *18* (7), 1–12. https://doi.org/10.3390/s18071986.

(5) OMSA. Nitrate-and-Nitrite-Fact-Sheet-2022_2. **2022**, No. 3, 438–444.

(6) Farsang, R.; Kovacs, Z.; Jarvas, G.; Guttman, A. Ultrahigh-Sensitivity Capillary Electrophoresis Analysis of Trace Amounts of Nitrate and Nitrite in Environmental Water Samples. *Separations*. 2022. https://doi.org/10.3390/separations9110333.

(7) Thipwimonmas, Y.; Jaidam, J.; Samoson, K.; Khunseeraksa, V.; Phonchai, A.; Thiangchanya, A.; Chang, K. H.; Abdullah, A. F.; Limbut, W. A Simple and Rapid Spectrophotometric Method for Nitrite Detection in Small Sample Volumes. *Chemosensors*. 2021. https://doi.org/10.3390/chemosensors9070161.

(8) Murray, E.; Roche, P.; Briet, M.; Moore, B.; Morrin, A.; Diamond, D.; Paull, B. Fully Automated, Low-Cost Ion Chromatography System for in-Situ Analysis of Nitrite and Nitrate in Natural Waters. *Talanta* **2020**, *216*, 120955. https://doi.org/https://doi.org/10.1016/j.talanta.2020.120955.

(9) Cox, R. D. Determination of Nitrate and Nitrite at the Parts per Billion Level by Chemiluminescence. *Anal. Chem.* **1980**, *52* (2), 332–335. https://doi.org/10.1021/ac50052a028.

(10) Zhang, M.; Yuan, D.; Huang, Y.; Chen, G.; Zhang, Z. Sequential Injection Spectrophotometric Determination of Nanomolar Nitrite in Seawater by On-Line Preconcentration with HLB Cartridge. *Acta Oceanol. Sin.* **2010**, *29* (1), 100–107. https://doi.org/10.1007/s13131-010-0012-4.

(11) Dallavalle, S.; Dobričić, V.; Lazzarato, L.; Gazzano, E.; Machuqueiro, M.; Pajeva, I.; Tsakovska, I.; Zidar, N.; Fruttero, R. Improvement of Conventional Anti-Cancer Drugs as New Tools against Multidrug Resistant Tumors. *Drug Resist. Updat.* **2020**, *50*. https://doi.org/10.1016/j.drup.2020.100682.

(12) Kopecka, J.; Trouillas, P.; Gašparović, A. Č.; Gazzano, E.; Assaraf, Y. G.; Riganti, C. Phospholipids and Cholesterol: Inducers of Cancer Multidrug Resistance and Therapeutic Targets. *Drug Resist. Updat.* **2020**, *49*. https://doi.org/10.1016/j.drup.2019.100670.

(13) Jigyasa; Pratibha; Rajput, J. K. Alkali Metal (Na/ K) Doped Graphitic Carbon Nitride (g-C3N4) for Highly Selective and Sensitive Electrochemical Sensing of Nitrite in Water and Food Samples. *J. Electroanal. Chem.* **2020**, *878*, 114605. https://doi.org/10.1016/j.jelechem.2020.114605.

(14) Nandi, I.; Rai, S. K.; Chandra, P. Talanta MOF-Based Nanocomposites as Transduction Matrices for Optical and Electrochemical Sensing. *Talanta* **2024**, *266* (P2), 125124. https://doi.org/10.1016/j.talanta.2023.125124.

(15) Ezhil Vilian, A. T.; Dinesh, B.; Muruganantham, R.; Choe, S. R.; Kang, S. M.; Huh, Y. S.; Han, Y. K. A Screen Printed Carbon Electrode Modified with an Amino-Functionalized Metal Organic Framework of Type MIL-101(Cr) and with Palladium Nanoparticles for Voltammetric Sensing of Nitrite. *Microchim. Acta* **2017**, *184* (12), 4793–4801. https://doi.org/10.1007/s00604-017-2513-8.

(16) Chen, Y. C.; Chiang, W. H.; Kurniawan, D.; Yeh, P. C.; Otake, K. I.; Kung, C. W. Impregnation of Graphene Quantum Dots into a Metal-Organic Framework to Render Increased Electrical Conductivity and Activity for Electrochemical Sensing. *ACS Appl. Mater. Interfaces* **2019**, *11* (38), 35319–35326. https://doi.org/10.1021/acsami.9b11447.

(17) Chen, H.; Yang, T.; Liu, F.; Li, W. Electrodeposition of Gold Nanoparticles on Cu-Based Metal-Organic Framework for the Electrochemical Detection of Nitrite. *Sensors Actuators, B Chem.* **2019**, *286* (March 2018), 401–407. https://doi.org/10.1016/j.snb.2018.10.036.

(18) Lin, P.; Chai, F.; Zhang, R.; Xu, G.; Fan, X.; Luo, X. Electrochemical Synthesis of Poly(3,4-Ethylenedioxythiophene) Doped with Gold Nanoparticles, and Its Application to Nitrite Sensing. *Microchim. Acta* **2016**, *183* (3), 1235–1241. https://doi.org/10.1007/s00604-016-1751-5.

(19) Rao, H.; Liu, Y.; Zhong, J.; Zhang, Z.; Zhao, X.; Liu, X.; Jiang, Y.; Zou, P.; Wang, X.; Wang, Y. Gold Nanoparticle/Chitosan@N,S Co-Doped Multiwalled Carbon Nanotubes Sensor: Fabrication, Characterization, and Electrochemical Detection of Catechol and Nitrite. *ACS Sustain. Chem. Eng.* **2017**, *5* (11), 10926–10939. https://doi.org/10.1021/acssuschemeng.7b02840.

(20) Kumar, A.; Purohit, B.; Mahato, K.; Roy, S.; Srivastava, A.; Chandra, P. Design and Development of Ultrafast Sinapic Acid Sensor Based on Electrochemically Nanotuned Gold Nanoparticles and Solvothermally Reduced Graphene Oxide. *Electroanalysis* **2020**, *32* (1), 59–69. https://doi.org/10.1002/elan.201900406.

(21) Fathy, M. M.; Elfiky, A. A.; Bashandy, Y. S.; Hamdy, M. M.; Elgharib, A. M.; Ibrahim, I. M.; Kamal, R. T.; Mohamed, A. S.; Rashad, A. M.; Ahmed, O. S.;

Elkaramany, Y.; Abdelaziz, Y. S.; Amin, F. G.; Eid, J. I. An Insight into Synthesis and Antitumor Activity of Citrate and Gallate Stabilizing Gold Nanospheres. *Sci. Rep.* **2023**, *13* (1), 1–11. https://doi.org/10.1038/s41598-023-29821-4.

(22) Shubhangi, N.; Kumari, R.; Rai, S. K.; Chandra, P. Electrochemical Assembly of Nickel Metal Organic Framework-Decorated Nanoimprinted Gold Dendrites as Peroxidase Mimic for High-Performance Hydrogen Peroxide Sensing. *ACS Appl. Nano Mater.* **2024**, *7* (1), 1388–1401. https://doi.org/10.1021/acsanm.3c05396.

(23) Zhou, P.; Cheng, J.; Yan, Y.; Xu, S.; Zhou, C. Ultrafast Preparation of Hydrophobic ZIF-67/Copper Mesh via Electrodeposition and Hydrophobization for Oil/Water Separation and Dyes Adsorption. *Sep. Purif. Technol.* **2021**, *272*, 118871. https://doi.org/https://doi.org/10.1016/j.seppur.2021.118871.

(24) Zhang, T.; Du, J.; Zhang, H.; Xu, C. In-Situ Growth of Ultrathin ZIF-67 Nanosheets on Conductive Ti@TiO2/CdS Substrate for High-Efficient Electrochemical Catalysis. *Electrochim. Acta* **2016**, *219*, 623–629. https://doi.org/https://doi.org/10.1016/j.electacta.2016.10.002.

(25) Worrall, S. D.; Mann, H.; Rogers, A.; Bissett, M. A.; Attfield, M. P.; Dryfe, R. A. W. Electrochemical Deposition of Zeolitic Imidazolate Framework Electrode Coatings for Supercapacitor Electrodes. *Electrochim. Acta* **2016**, *197*, 228–240. https://doi.org/https://doi.org/10.1016/j.electacta.2016.02.145.

(26) Han, H.; Yuan, X.; Zhang, Z.; Zhang, J. Preparation of a ZIF-67 Derived Thin Film Electrode via Electrophoretic Deposition for Efficient Electrocatalytic Oxidation of Vanillin. *Inorg. Chem.* **2019**, *58* (5), 3196–3202. https://doi.org/10.1021/acs.inorgchem.8b03281.

(27) Feng, S.; Li, X.; Huo, J.; Li, Q.; Xie, C.; Liu, T.; Liu, Z.; Wu, Z.; Wang, S. Controllable Synthesis of CoS2@N/S-Codoped Porous Carbon Derived from ZIF-67 for as a Highly Efficient Catalyst for the Hydrogen Evolution Reaction. *ChemCatChem* **2018**, *10* (4), 796–803. https://doi.org/10.1002/cctc.201701353.

(28) Lin, J.; Gao, X.; Gong, L.; Zhang, X.; Li, T.; Zhao, F.; Zeng, B. An Electrochemically Fabricated ZIF-67/[HOEMIM]BF4 Coating for the Solid-Phase Microextraction and Detection of Polycyclic Aromatic Hydrocarbons. *Anal. Methods* **2023**, *15* (37), 4883–4891. https://doi.org/10.1039/d3ay01174g.

(29) Jee, H.-W.; Paeng, K.-J.; Myung, N.; Rajeshwar, K. Electrochemical Deposition of a Metal–Organic Framework and Subsequent Conversion to Cobalt Selenide. *ACS Appl. Electron. Mater.* **2020**, *2* (5), 1358–1364. https://doi.org/10.1021/acsaelm.0c00142.

(30) Nguyen, A. N.; Tran, N. M.; Yoo, H. Direct Growth and Post-Treatment of Zeolitic Imidazolate Framework-67 on Carbon Paper: An Effective and Stable Electrode System for Electrocatalytic Reactions. *J. Mater. Chem. A* **2022**, *10* (39), 20770–20778. https://doi.org/10.1039/d2ta03922b.

(31) Zhou, P.; Yan, Y.; Cheng, J.; Zhou, C. Stainless Steel Mesh Coated with Defect

Engineered ZIF-67 toward PH-Switchable Wettability and Efficient Organic Liquids Separation. *Colloids Surfaces A Physicochem. Eng. Asp.* **2022**, *634*, 127950. https://doi.org/https://doi.org/10.1016/j.colsurfa.2021.127950.

(32) Zhao, S.; Chen, J. Metal Organic Framework-Derived Ni/Zn/Co/NC Composites as Efficient Catalyst for Oxygen Evolution Reaction. *J. Porous Mater.* **2019**, *26* (2), 381–387. https://doi.org/10.1007/s10934-018-0612-5.

(33) Huang, H.; Zhao, Y.; Bai, Y.; Li, F.; Zhang, Y.; Chen, Y. Conductive Metal–Organic Frameworks with Extra Metallic Sites as an Efficient Electrocatalyst for the Hydrogen Evolution Reaction. *Adv. Sci.* **2020**, *7* (9), 1–9. https://doi.org/10.1002/advs.202000012.

(34) Yuan, M.; Wang, R.; Sun, Z.; Lin, L.; Yang, H.; Li, H.; Nan, C.; Sun, G.; Ma, S. Morphology-Controlled Synthesis of Ni-MOFs with Highly Enhanced Electrocatalytic Performance for Urea Oxidation. *Inorg. Chem.* **2019**, *58* (17), 11449–11457. https://doi.org/10.1021/acs.inorgchem.9b01124.

(35) Kitchamsetti, N.; Ramteke, M. S.; Rondiya, S. R.; Mulani, S. R.; Patil, M. S.; Cross, R. W.; Dzade, N. Y.; Devan, R. S. DFT and Experimental Investigations on the Photocatalytic Activities of NiO Nanobelts for Removal of Organic Pollutants. *J. Alloys Compd.* **2021**, *855*, 157337. https://doi.org/https://doi.org/10.1016/j.jallcom.2020.157337.

(36) Bagus, P. S.; Nelin, C. J.; Brundle, C. R.; Crist, B. V.; Ilton, E. S.; Lahiri, N.; Rosso, K. M. Main and Satellite Features in the Ni 2p XPS of NiO. *Inorg. Chem.* **2022**, *61* (45), 18077–18094. https://doi.org/10.1021/acs.inorgchem.2c02549.

(37) Chen, H.; Wu, X.; Zhao, R.; Zheng, Z.; Yuan, Q.; Dong, Z.; Gan, W. Preparation of Reduced Graphite Oxide Loaded with Cobalt(II) and Nitrogen Co-Doped Carbon Polyhedrons from a Metal-Organic Framework (Type ZIF-67), and Its Application to Electrochemical Determination of Metronidazole. *Microchim. Acta* **2019**, *186* (9). https://doi.org/10.1007/s00604-019-3737-6.

(38) Sun, M.; Xu, H.; Meng, Y.; Chen, X.-M.; Lu, M.; Yu, H.; Zhang, C.-B. Facile Design and Synthesis of a Nickel Disulfide/Zeolitic Imidazolate Framework-67 Composite Material with a Robust Cladding Structure for High-Efficiency Supercapacitors. *RSC Adv.* **2022**, *12* (37), 23912–23921. https://doi.org/10.1039/D2RA04317C.

(39) Gougis, M.; Pereira, A.; Ma, D.; Mohamedi, M. Simultaneous Deposition of Cerium Oxide and Gold Nanostructures-Characterization and Analytical Properties toward Glucose Electro-Oxidation and Sensing. *RSC Adv.* **2014**, *4* (75), 39955–39961. https://doi.org/10.1039/c4ra05374e.

(40) Casella, I. G.; Gatta, M. Study of the Electrochemical Deposition and Properties of Cobalt Oxide Species in Citrate Alkaline Solutions. *J. Electroanal. Chem.* **2002**, *534* (1), 31–38. https://doi.org/10.1016/S0022-0728(02)01100-2.

(41) Jayaraman, T. R.; Venkatesan, V. K.; Udupa, H. V. K. Cyclic Voltammetric

Studies of Electroless Cobalt in NaOH. *Electrochim. Acta* **1975**, *20* (3), 209–213. https://doi.org/https://doi.org/10.1016/0013-4686(75)85026-2.

(42) Kumari, R.; Chandra, P. Electrochemical Nano-Imprinting of Trimetallic Dendritic Surface for Ultrasensitive Detection of Cephalexin in Pharmaceutical Formulations. *Pharmaceutics* **2023**, *15* (3). https://doi.org/10.3390/pharmaceutics15030876.

(43) Mandal, R.; Baranwal, A.; Srivastava, A.; Chandra, P. Evolving Trends in Bio/Chemical Sensor Fabrication Incorporating Bimetallic Nanoparticles. *Biosens. Bioelectron.* **2018**, *117*, 546–561. https://doi.org/https://doi.org/10.1016/j.bios.2018.06.039.

(44) Hoegger, D.; Morier, P.; Vollet, C.; Heini, D.; Reymond, F.; Rossier, J. S. Disposable Microfluidic ELISA for the Rapid Determination of Folic Acid Content in Food Products. *Anal. Bioanal. Chem.* **2007**, *387* (1), 267–275. https://doi.org/10.1007/s00216-006-0948-6.

(45) Liu, H. Y.; Wen, J. J.; Xu, H. X.; Qiu, Y. Bin; Yin, Z. Z.; Li, L. H.; Gu, C. C. Development of a Copper-Based Metal Organic Electrode for Nitrite Sensing. *J. AOAC Int.* **2021**, *104* (1), 157–164. https://doi.org/10.1093/jaoacint/qsaa089.

(46) Li, X.; Zou, N.; Wang, Z.; Sun, Y.; Li, H.; Gao, C.; Wang, T.; Wang, X. An Electrochemical Sensor for Determination of Nitrite Based on Au Nanoparticles Decorated MoS2 Nanosheets. *Chem. Pap.* **2020**, *74* (2), 441–449. https://doi.org/10.1007/s11696-019-00885-9.

(47) Jian, J. M.; Fu, L.; Ji, J.; Lin, L.; Guo, X.; Ren, T. L. Electrochemically Reduced Graphene Oxide/Gold Nanoparticles Composite Modified Screen-Printed Carbon Electrode for Effective Electrocatalytic Analysis of Nitrite in Foods. *Sensors Actuators, B Chem.* **2018**, *262*, 125–136. https://doi.org/10.1016/j.snb.2018.01.164.

(48) Kumari, R.; Dkhar, D. S.; Chandra, P. Electrochemically Nanotuned Surface Comprising 3D Bimetallic Dendrites Fabricated on MWCNT for Detection of 1,4-Dioxane in Water. *Microchem. J.* **2023**, *191*, 108845. https://doi.org/https://doi.org/10.1016/j.microc.2023.108845.

(49) Chang, T. E.; Chuang, C. H.; Kung, C. W. An Iridium-Decorated Metal–Organic Framework for Electrocatalytic Oxidation of Nitrite. *Electrochem. commun.* **2021**, *122* (December 2020), 106899. https://doi.org/10.1016/j.elecom.2020.106899.

(50) Li, X.-S.; Zou, X.; Chen, W.-Y.; Sun, Q.; Gao, E.-Q. High Sensitivity Detection of Nitrite Electrochemical Sensor Modified with MOF Composite Materials. *J. Electrochem. Soc.* **2023**, *170* (12), 127514. https://doi.org/10.1149/1945-7111/ad162f.

(51) Gupta, V. K.; Khalilzadeh, M. A.; Rudbaraki, A.; Agarwal, S.; Yola, M. L.; Atar, N. Fabrication of Highly Sensitive Nitrite Electrochemical Sensor in Foodstuff Using Nanostructure Sensor. *Int. J. Electrochem. Sci.* **2017**, *12* (5), 3931–3940.

https://doi.org/10.20964/2017.05.72.

(52) Feng, X. Z.; Ferranco, A.; Su, X.; Chen, Z.; Jiang, Z.; Han, G. C. A Facile Electrochemical Sensor Labeled by Ferrocenoyl Cysteine Conjugate for the Detection of Nitrite in Pickle Juice. *Sensors (Switzerland)* **2019**, *19* (2). https://doi.org/10.3390/s19020268.

(53) Wang, Y. C.; Chen, Y. C.; Chuang, W. S.; Li, J. H.; Wang, Y. Sen; Chuang, C. H.; Chen, C. Y.; Kung, C. W. Pore-Confined Silver Nanoparticles in a Porphyrinic Metal-Organic Framework for Electrochemical Nitrite Detection. *ACS Appl. Nano Mater.* **2020**, *3* (9), 9440–9448. https://doi.org/10.1021/acsanm.0c02052.

(54) Lu, S.; Jia, H.; Hummel, M.; Wu, Y.; Wang, K.; Qi, X.; Gu, Z. Two-Dimensional Conductive Phthalocyanine-Based Metal-Organic Frameworks for Electrochemical Nitrite Sensing. *RSC Adv.* **2021**, *11* (8), 4472–4477. https://doi.org/10.1039/d0ra10522h.

Chapter Appendix

Table 4.2. *Detailed report on MOF and non-MOF-based sensors for nitrite sensing.*

S.No.	Fabricated probe surface	Technique used	Fabrication strategy	Number of wet chemistry steps involved	Total fabrication time	Fabrication temp	LDR	LOD	Response Time	Real Sample used	Ref.
1.	Ni-HHTP@MWCNTs	DPV	A composite comprising of HHTP, $Ni(OAc)_2.4H_2O$ and MWCNTs was prepared through the hydrothermal method which was later coated on a GCE surface to form the final sensing probe.	1	16 hours,	85 °C	1-10000 μM	0.95 μM	N.R.	Tap and river water	[50]
2	CdO/SWCNTs/1-3-MBIB/CPE	CA, SWV	A mixture of ionic liquid binder, liquid paraffin, CdO/SWCNTs and pure graphite powder was prepared and homogenized. Then, it was packed within a glass tube to form the CdO/SWCNTs/1-3MBIB/CPE.	0	3 hours	RT	0.1-900 μM	0.07 μM	N.R.	Sausage, pickled vegetables	[51]
3.	GCE/MoS2/AuNPs	CA	GCE/MoS2/AuNPs were functionalized on a clean GCE surface. MoS2 was dropcasted initially on the GCE surface followed by electrodeposition of AuNPs.	0	>2 hours	RT	10-2100 µM	0.09 µM	N.R.	river and drinking water	[46]
4.	Fc-ECG/SPE	DPV	Initially, $Fc(Cys)_2$ was dissolved in acetonitrile. Similarly, Fc-ECG stock solution was prepared by dissolving in Milli-Q water. The sensor was prepared by dropcasting these materials onto SPE surface	0	30 minutes	RT	1.0–50 $\mu mol \cdot L^{-1}$	0.3 $\mu mol \cdot L^{-1}$	>5 minutes	Pickle juice	[52]
5.	Na/K doped carbon-nitride	LSV	A cleaned GCE electrode was dropcasted with calculated volumes of homogeneous	3	8.5 hours	70 ° C followed by 550 ° C	10 µM to 2 mM	1.9 µM	N.R.	Water and food	[13]

			solutions of Na/K-doped carbon nitride								
6.	GO-CS-AuNPs/GCE	CA	The GCE surface was initially drop coated with a solution of CS-GO and allowed to dry at RT. It was followed by electrodeposition of the surface with AuNPs to form the final sensor probe.	2	>23 for CS-GO synthesis followed by 30 min. for AuNP deposition	80 °C for the hummer's method	0.9 µM to 18.9 µM	0.3 µM	N.R.	N.R.	[4]
7.	Fe_2O_3/rGO	DPV	A dispersed mixture of Fe_2O_3/rGO composite was dropped onto GCE electrode surface and dried on RT to fabricate the final sensing surface.	2	>10.5 hrs	170 °C followed by 80 °C	5.0×10^{-8} to 7.8×10^{-4} M	1.5×10^{-8} M	N.R.	Tap water	[2]
8.	ERGOs/AuNP	DPV	SPCE was used as a WE. It was adorned with electrodeposited ERGO/AuNPs by scanning potential between 0 V to -1.5V for 15 cycles in a solution containing 1:1 v/v GO and $[AuCl_4]^-$solution.	0	>2 hrs	RT	1–6000 µM	0.13 µM	N.R.	Packaged drinking water, processed meats, aquatic products	[47]
					MOF -BASED NITRITE SENSORS						
9.	Pd/NH_2-MIL-101(Cr)	SWV and CV	SPCE was chosen as the working electrode which was dropcoated with Pd/NH_2-MIL-101(Cr) dispersion mixture.		>31 hours	160 °C for MOF synthesis followed by 200 °C for activation.	5 to 150 nM	1.3 nM	N.R.	Sausage and pickle samples.	[15]
10.	Cu-MOF/Au	CA	A GCE working electrode was dropcoated with Cu-MOF aqueous suspension. It was followed by potentiostatic electrodeposition of AuNPs.	1	>32 hours	RT synthesis of Cu-MOF followed by drying at 80 °C	0.1–4000 and 4000–10000 µM	82 nM	N.R.	River water	[17]
11.	GQD-PCN-222 (Zr-based MOF)	CA	Fluorine-doped tin oxide conducting glass substrates were chosen as the WE. GQD-PCN-222 thin films were prepared by dispersing initial sample pellets into acetone	1	>7 days	Pellet drying at 80 °C	40–18 000 µM	6.4 µM	N.R.	N.R.	[16]

			followed by dropcasting on the WE surface.								
12.	Zr-MOF	CA	A fluorine doped tin oxide conducting glass substrate WE was dropped with a thin-film of MOF/Ag composite dispersed in acetone. The deposition procedure was iterated thrice to fabricate the final sensing probe.	2	>66 hours on material preparation followed by film deposition on substrate	Synthesis at 60 °C followed by post synthetic drying at 80 °C.	Upto 2.0 mM	9.1 µM	N.R.	Tapwater, lake water, and rain water	[53]
13.	Iridium-decorated UiO-66	CA	The nodes of the UiO-66 were introduced with iridium sites through solvothermal approach. Further, a thin film of the dispersed Ir-UiO-66 in acetone was casted onto the surface of FTO substrate to form the WE.	2	>20 hrs	Varying temperatures ranging from 25 °C to 130 °C	0 mM to 0.2 mM	0.41 µM	60 s	N.R.	[49]
14.	Cu-MOF/Au@Pt/GCE	CA	The prepared Cu-MOF was dispersed onto the surface on a GCE WE and dried under UV lamp. Further, the modified electrode was electrodeposited with Au@P NPs by CV to obtain the final WE.	2	>20 hrs for Cu-MOF preparation	RT	0.0001–12 mM	72 nM	5s	Ham sausage sample	[45]
15.	NiPc-MOFs	DPV, CA	Ni phthalocyanine MOF synthesized through the solvothermal route was casted onto a GCE surface sealed with nafion.	1	>12 hrs for MOF-nanosheet synthesis	70 ℃	0.01 mM to 11 500 mM	2.3 µM	6 s	Tap water	[54]
16.	***Ni-MOF/ Co-MOF/AuNPs***	***LSV, CA***	***Ni-MOF and Co-MOFs were synthesized through the electrochemical approach and stacked over one another. The system was further functionalized with AuNPs.***	***1***	***1000 s for MOF deposition and 15 minutes for AuNP drying.***	***RT***	***0.01-1 µM to 10-1000 µM***	***4.2 ± 0.0003 nM***	***<1.5 s for a range of concentartions***	***Pond water, Tap water***	***Our work***

Abbreviations: *MWCNTs: Multiwalled Carbon Nanotubes; DPV: Differential Pulse Voltammetry; CdO: Cadmium oxide; SWV: Square wave voltammetry; MoS2: Molybdenum oxide; AuNPs: Gold nanoparticle; CA: chronoamperometry; SPE: Screen Printed Electrode; rGO: reduced Graphene oxide; CV: cyclic voltammetry; LSV: linear sweep voltammetry; GCE: Glassy carbon electrode*

Software final DART code for NitriSens Application

```
// Automatic FlutterFlow imports
import '/flutter_flow/flutter_flow_theme.dart';
import '/flutter_flow/flutter_flow_util.dart';
import 'index.dart'; // Imports other custom actions
import '/flutter_flow/custom_functions.dart'; // Imports custom functions
import 'package:flutter/material.dart';
// Begin custom action code
// DO NOT REMOVE OR MODIFY THE CODE ABOVE!


Future<double> finalCode(
  BuildContext context,
  double? currrent,
) async {
  // get the result of x=(current-a)/b
  if (currrent != null && 0.691 <= currrent && currrent <= 1.370) {
    double x = ((currrent - 0.691) / 0.0707);
    //return x * 1000000000;//
    return double.parse(x.toStringAsFixed(2));
  } else if (currrent != null && 1.371 <= currrent && currrent <= 6.68) {
    double x = ((currrent - 1.303) / 0.00537);
    //return x * 1000000000;//
    return double.parse(x.toStringAsFixed(2));
  } else {
    return 0.0;
  }
}
```